Optimising Radiotherapy-Immunotherapy Combinations to Improve Glioblastoma Treatment via Mathematical Modelling

Daniel Golshmid
Department of Biochemical Engineering

Supervised by:
Dr. David Morselli and Dr. Carina Dunlop
Department of Mathematics

LAIDLAW SCHOLARS

UCL

Abstract

Glioblastoma (GBM) is the most common and lethal primary malignant brain cancer. It has limited therapeutic options and a poor prognosis driven largely by considerable alterations within the tumour microenvironment and the tumour's extraordinary capacity for self-renewal and repopulation after treatment. Standard GBM treatment remains fractionated radiotherapy, though immunotherapy has recently emerged as a cornerstone of brain tumour treatment. However, how radiotherapy-immunotherapy combinations could be optimised to maximise synergistic benefit and improve patient outcomes remains poorly understood. Mechanism-based mathematical modelling is one promising approach for systematically investigating scheduling combinations to identify treatment strategies that maximise positive outcomes and warrant further investigation in clinical trials. In this study, we develop a comprehensive modelling and computational framework focusing on interactions between tumour and immune cells, as mediated by several cytokines and the immune checkpoint inhibitor anti-PD-L1. The spatially reduced ordinary differential equation (ODE) model was analysed, demonstrating that combining radiotherapy and immunotherapy offers clear advantages in controlling tumour growth compared with either therapy alone. We then performed an optimisation analysis focusing on radiation fractionation, dose, and timing relative to immunotherapy to identify specific treatment strategies that improve predicted outcomes while minimising unnecessary radiation exposure. Several specific scheduling strategies showed the potential to significantly improve outcomes over current GBM treatment. Following a sensitivity analysis quantifying each parameter's influence on tumour mass progression, we present a structurally simplified model designed to reproduce the outcomes of the full model with high accuracy. This simplified model can be applied in clinical and research settings to accommodate patient-specific cases and scenarios, providing information to support treatment-planning decisions.

Contents

1 Introduction

Glioblastoma (GBM) is the most common and aggressive primary malignant brain tumour, making up 16% of all primary brain tumours and 54% of all gliomas [77], with a dismal median survival of 12-15 months [78]. It is a recurrent cancer that, despite extensive research, remains resistant to practically all therapeutic approaches due to its cellular and molecular heterogeneity, comprising various cell populations within a dynamic tumour microenvironment (TME) [76, 98]. Glioma stem cells (GSCs) play a particularly pivotal role in cancer relapse and chemotherapy resistance due to their self-renewal and adaptability capabilities [14, 19]. Consequently, complete surgical removal of the tumour mass is impossible, as residual GSCs and infiltrative tumour cells frequently drive more aggressive recurrence [24, 105]. For this reason, although standard of care typically involves maximal safe surgical resection followed by adjuvant chemotherapy with temozolomide (TMZ) [84], radiotherapy (RT) stands as the cornerstone of GBM management. RT involves the fractioned administration of ionizing radiation (IR) aimed precisely at the tumour. IR causes damage to DNA of cancerous cells and changes in the inflammatory TME, resulting in tumour shrinkage [88]. Radiation has also been shown to activate the antitumour immunity, despite the particular sensitivity of lymphocytes to IR [47, 57, 100]. However, RT also faces significant challenges due to the ability of GSCs to promote radioresistance through highly efficient DNA damage response [83], contributing to the almost inevitable recurrence of GBM following IR treatment [101].

Immunotherapies, a class of treatments that help the immune system fight cancer, have historically been excluded from treating intracranial malignant diseases such as GBM, due to the notion that the blood brain barrier (BBB) prohibits the access of immune mediators to the brain [21, 5]. However, recent studies have shown that brain malignancies compromise the BBB, an effect further strengthened by IR, positioning immunotherapy as an emerging fourth pillar in GBM treatment [21, 32, 40]. A key area of investigation is the combined effects of radiotherapy and immunotherapy, and whether their immunogenic effects might act synergistically to improve patient outcomes. Among the immunotherapies that hold potential for this improvement when combined with radiotherapy, the anti-PD-L1 drug, which targets the programmed death-ligand 1 (PD-L1), is of particular interest. PD-L1 and its receptor, programmed death 1 (PD-1), are frequently upregulated in cancers, where their interaction inhibits cytotoxic T-cell function, helping tumour cells to evade immune control [35]. This upregulation effect is enhanced following RT [3, 23], thereby suppressing the antitumour activity of CD4+ T helper 1 (Th1) and CD8+ cells. Therefore, there's a strong rationale for combining RT and anti-PD-L1 in the treatment of GBM [3, 23]. Although recent research has demonstrated that this synergistic effect exists [23, 60, 107], and that anti-PD-L1 sensitizes tumours to RT, precisely how RT-IT combinations, including their scheduling and dosing, could be optimised to maximise this combined benefit and improve treatment outcomes remains poorly understood.

Mathematical modelling of the GBM microenvironment is a promising approach for capturing the complexity of this biological system, offering insights that can inform and guide treatment decisions. Mathematical models can enhance our understanding of the dynamic processes within the TME that drive cancer proliferation, particularly those that would otherwise remain elusive from experimental data alone [41, 15]. While existing clinical methods can reveal surface-level changes in tumours, extensive real-time measurement of all TME components remains impractical [25]. Modelling instead provides a means of exploring theoretical, as-yet-untested treatments for GBM, such as predicting patient out-

comes across a wide range of RT-IT treatment combinations. It can thus help optimise treatment protocols and narrow down promising candidates for further investigation in clinical trials.

Formulating mathematical models as a system of ordinary differential equations (ODEs), each describing the temporal evolution of a specific TME component, is particularly well suited to capturing the highly dynamic, multi-population interactions that characterise GBM [2]. By setting aside spatial complexity, such models remain computationally tractable, enabling the systematic screening of a wide range of RT–IT treatment combinations and yielding robust and comprehensive predictions of the resulting treatment outcomes.

In this study, we present a comprehensive mathematical model of the complex interaction GBM microenvironment and characterise their response to theoretical RT-IT therapy combinations. The model describes the dynamic interplay among differentiated tumour cells, GSCs, immune cells and a set of cytokines. Our methodology incorporates model calibration from experimental results, ensuring that the model accurately mirrors the observed biological dynamics. It is then used to analyse the changes that occur in the TME in response to different treatment scenarios, helping to identify promising treatment strategies for GBM and their potential to improve patient outcomes compared to standards of care. A sensitivity analysis is also performed to investigate how patient-specific factors could influence treatment choices across different patient-specific cases and scenarios, providing information to support treatment-planning decisions in clinical and research settings.

2 Methods

2.1 The Mathematical Model

The aim of our mathematical model is to describe a generalised version of the complicated biological processes in the GBM tumour microenvironment. The model describes the effect of interactions between glioma cells (differentiated tumour cells, GSCs, and radiation-damaged cells) and the immune system, which includes dendritic cells, macrophages, T lymphocytes ($CD4^+$, $CD8^+$, Treg cells), and a collection of six tumour-related cytokines (IL-2, IL-10, IL-12, TGF-β, IFN-γ, and IL-1β). We shall combine MDSCs and M2 macrophages, and denote them by M due to their comparable anti-inflammatory cytokine release phenotype. A schematic diagram depicting the basis for the mathematical model is shown in Figure 1.

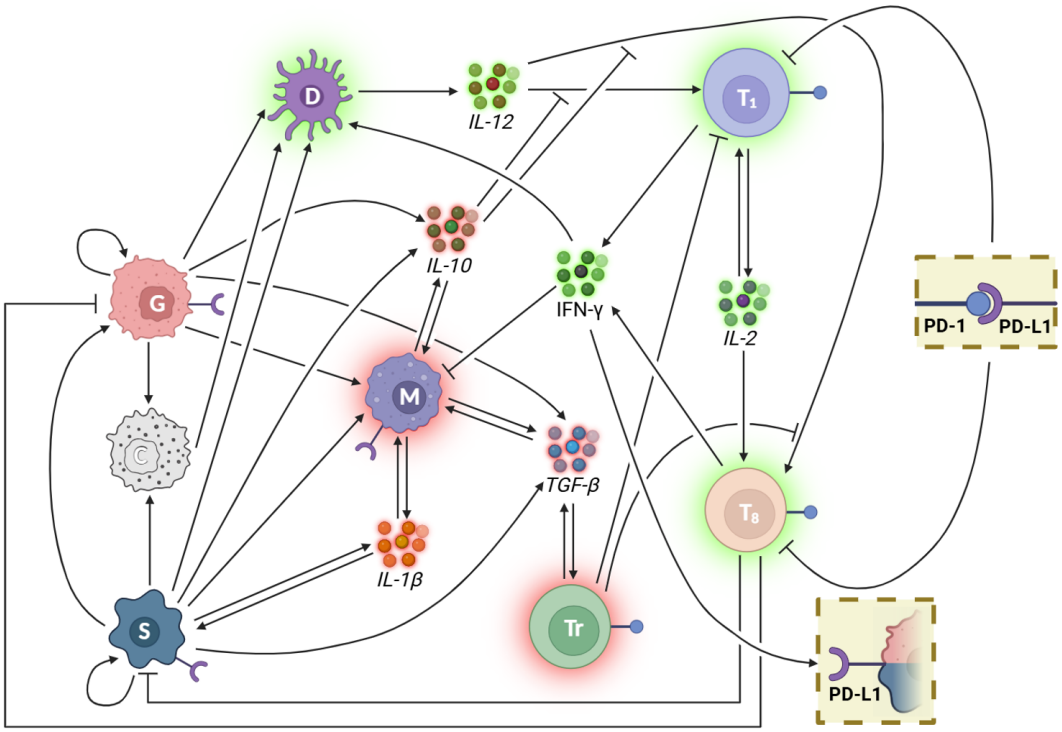

Figure 1 Tumour immune microenvironment interactions. Sharp arrows indicate proliferation/activation, blocked arrows indicate killing/blocking. Green halo indicates a tumour-suppressive component, red halo indicates a tumour-promoting component. G: differentiated cancer cells; S: glioma stem cells; C: radiation-damaged cancer cells; D: dendritic cells; M : MDSC and M2 macrophages; T1: CD4+ Th1 cells; T8: CD8+ T cells; Tregs: T regulatory cells; T1, T8, Tr cells express PD-1; G, S, M cells express PD-L1.

We follow the derivation of the LQ model presented by Sachs et al [85] to describe the radiation response of a tumour. We model radiation response with distinct survival parameters for differentiated tumour cells, GSCs, and immune cells to capture their differing radiosensitivities. Full derivation of the radiation modelling is presented in Appendix A.

The model was developed as a non-spatial system of ODEs describing interactions within the tumour microenvironment and the resulting changes in modelled population masses. A constant tumour volume of 27 mL was assumed, corresponding to the median GBM tumour volume at the time of detection reported in [74]. It should be noted that the

somewhat arbitrary choice of volume value does not affect the simulated resulting trends. The complete ODE model, including all equations and their justification, is presented in Appendix B.

2.2 Parameter Selection

Determining and accurately estimating the numerical parameters is crucial for developing a robust and reliable predictive model. However, for most of the quantities involved, parameter values are difficult to obtain through direct measurements (in vivo) and must be inferred from in vitro experiments or mathematical estimations. Where possible, we used parameter values outlined in literature and estimated the remaining parameters by utilising results in experimental studies based on certain assumptions. Full details of the parameter estimation methodology are provided in Appendix C. A summary of the parameter values used in the model equations is presented in Table 1 in Appendix D. It is important to note that parameter estimations are mere approximations within a rough range. The main conclusions in the study are not sensitive to the parameter values. A sensitivity analysis that examined the responsiveness of model predictions to variations in parameter values is detailed in a subsequent section.

2.3 Numerical Method

The model equations were numerically solved in MATLAB using a variable-step, variable-order (VSVO) solver based on numerical differentiation formulas (NDFs) of orders 1 to 5. This method was chosen to effectively handle the stiffness inherent in the model equations, which arises from the presence of processes occurring on different timescales.

To simulate normal tumour growth under immune surveillance, the initial conditions were selected to correspond to a physiologically plausible steady state prior to tumour onset. These values were determined following numerical testing and are given below in grams:

$$
\begin{aligned}
&D = 1.9 \times 10^{-6}, \quad T_1 = 2.5 \times 10^{-5}, \quad T_8 = 1.4 \times 10^{-5}, \quad T_r = 2.4 \times 10^{-2}, \\
&M = 1.8 \times 10^{-4}, \quad G = 0.866, \quad S = 2.9 \times 10^{-3}, \quad C = 0, \\
&I_{12} = 3.4 \times 10^{-12}, \quad I_2 = 8.7 \times 10^{-13}, \quad T_\beta = 2.9 \times 10^{-7}, \quad I_{10} = 6.6 \times 10^{-10}, \\
&I_\beta = 3.3 \times 10^{-11}, \quad I_\gamma = 6.6 \times 10^{-13}, \quad L = 4.95 \times 10^{-10}
\end{aligned}
$$

We note that the choices of initial conditions did not affect the long term simulation results.

3 Results and Discussion

3.1 Dynamics of TME responses

To analyse the dynamic changes in the TME driven by tumour growth, we solved the model equations using the parameter values and initial conditions described above. We first simulated the system in the absence of any therapy, with results expressed in concentration units (g/cm^3) for all cell types and cytokines, as shown in Figure 2.

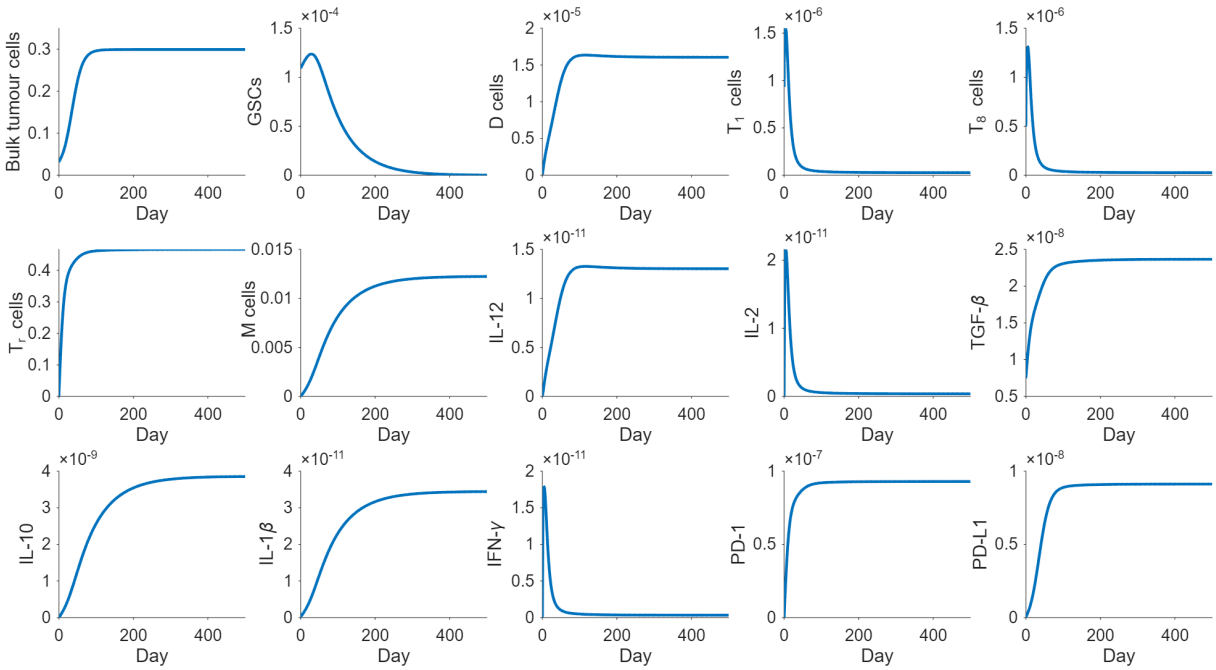

Figure 2 Simulated dynamics of the tumour microenvironment in the absence of therapy. Concentrations (g/cm^3) of cells and cytokines, together with PD-1 and PD-L1, over 500 days of untreated tumour growth.

Bulk tumour cell concentration increases steadily to a maximum of 0.299 g/cm^3 (interchangeable with mass under the constant-volume assumption), before reaching a steady state and remaining approximately constant thereafter. During the initial phase of tumour growth, CD4$^+$ Th1 (T1) and CD8$^+$ T cells (T8) briefly increase before dropping sharply as tumour mass expands, with IL-2 and IFN-γ production following a similar trajectory, indicative of progressive immune exhaustion as the tumour establishes dominance over the GBM TME. By contrast, M cells, dendritic cells (D), regulatory T cells (Tr), and the tumour-promoting cytokines IL-12, TGF-β, IL-10, and IL-1β all increase substantially alongside tumour growth. Correspondingly, PD-L1 (expressed on tumour and M cell surfaces) and PD-1 (expressed on regulatory T cells) both rise in parallel. GSCs initially expand while bulk tumour cells have not yet dominated the available space, but subsequently decline as differentiated cells proliferate further, reflecting resource competition between the two tumour subpopulations for the shared carrying capacity.

Building on this baseline, we next simulated the model's response to a single 5 Gy radiation dose, in order to characterise how radiotherapy perturbs tumour and immune cell dynamics (Figure 3, same units as Figure 2).

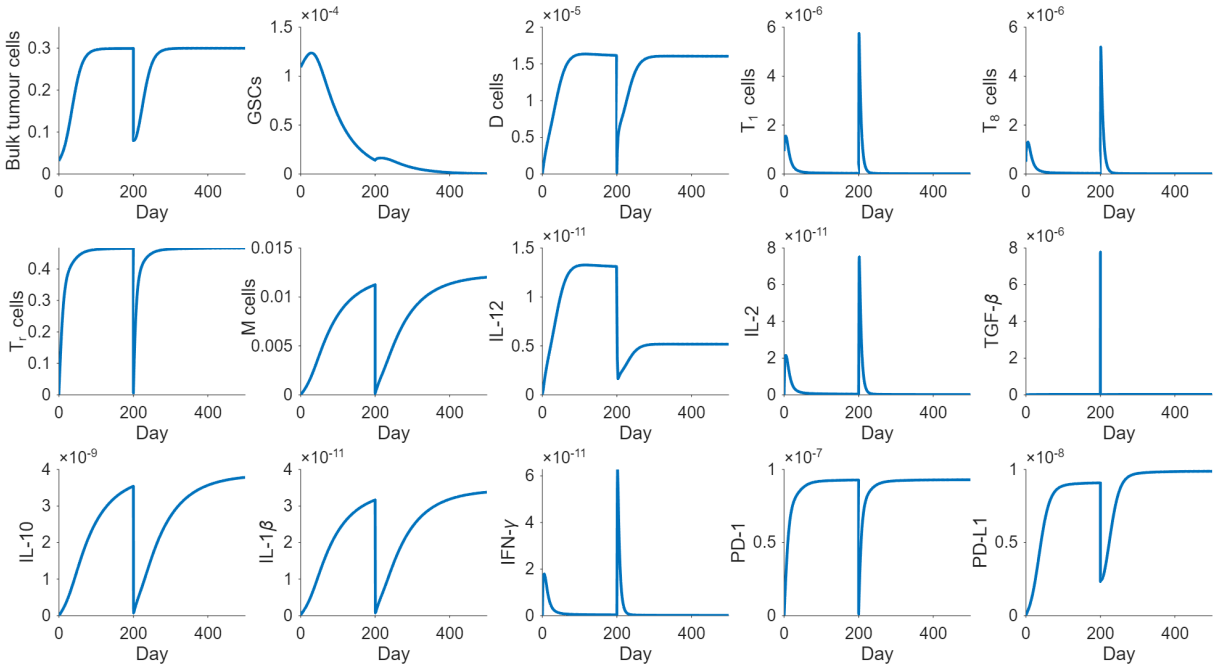

Figure 3 Simulated dynamics of the tumour microenvironment following a single 5 Gy radiotherapy dose, administered once the tumour has reached its pre-treatment steady state (day 200), in ng/cm^3.

Immediately following irradiation, bulk tumour cell mass declines sharply, as do all other cell populations, though GSCs show the smallest relative decline, consistent with their radioresistant phenotype. Following this acute depletion, bulk tumour cells, D cells, and Tr cells all recover to their pre-radiation steady-state levels. M cells, along with IL-10 and IL-1β, instead stabilise at a higher steady state than before treatment, suggesting a tumour-promoting consequence of radiation-induced changes in the TME. CD4$^+$ (T1) and CD8$^+$ (T8) T cells show a pronounced, transient increase following irradiation, reflecting a short-lived strengthening of the adaptive immune response. This response is not sustained, however, as the tumour re-establishes suppression of the conventional T-cell-mediated immunity. This surge in T1 and T8 cells drives a corresponding increase in IL-2 and IFN-γ production, while TGF-β also rises, consistent with a radiation-induced fibroblast stress response. Unlike these cytokines, IL-12 fails to return to its pre-radiation level, reflecting sustained suppression of IL-12 production by dendritic cells following irradiation. Notably, while PD-1 returns to its pre-radiation level after treatment, PD-L1 stabilises at a higher steady state, driven by the expanded M cell population that expresses it.

To understand how immunotherapy affects TME dynamics, we simulated an intravenous injection of anti-PD-L1 (administered systemically, prior to crossing the BBB) at a dose of 900 ng/cm^3 relative to tumour volume (Figure 4).

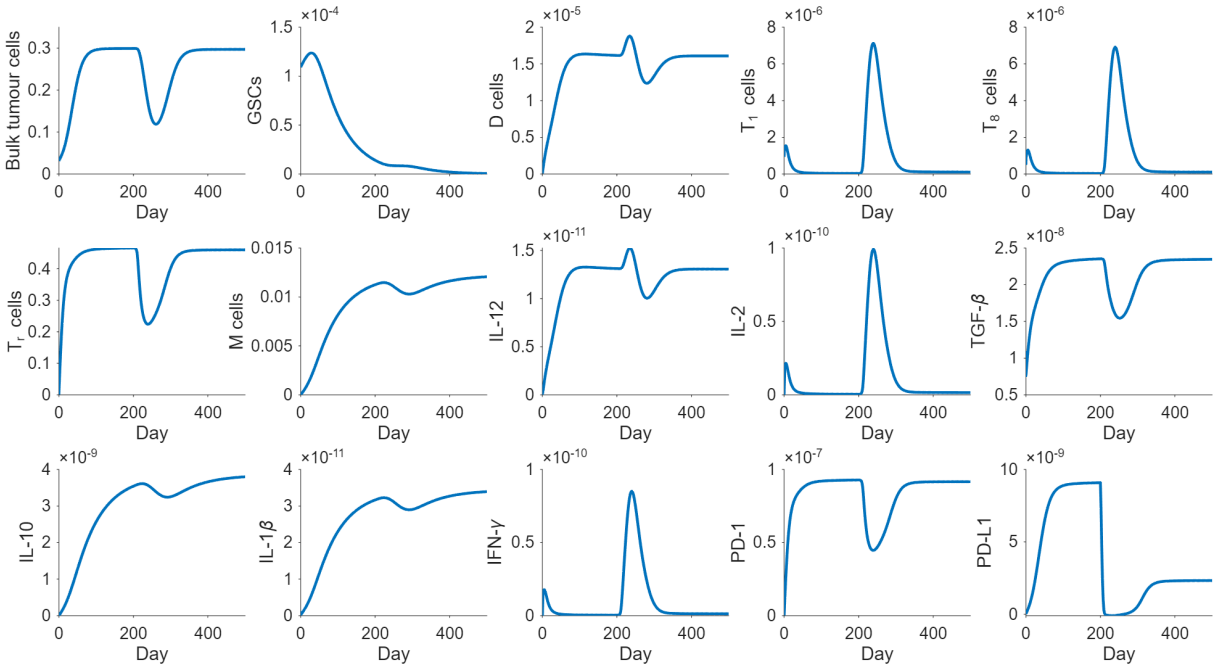

Figure 4 Simulated dynamics of the tumour microenvironment following administration of anti-PD-L1 immunotherapy at 900 ng/cm^3 at day 200, in ng/cm^3.

As expected, immunotherapy causes a sharp decrease in available PD-L1, thereby limiting tumour cells' capacity for immune evasion. Consequently, the levels of T1 and T8 cells actively engaged in antitumour immune suppression increase, with this response both larger in magnitude and more sustained than the transient spike observed following radiotherapy. As a result, bulk tumour cell levels undergo a marked decrease, before the tumour eventually overcomes this immune response and returns to its original high steady-state level. M cells, dendritic cells, and the cytokines IL-12, IL-10, and IL-1β all show fluctuations in response to immunotherapy administration, further reflecting the complex, interconnected dynamics of the TME under therapeutic interventions.

These observations raise the question of whether the combined effects of radiotherapy and immunotherapy on the TME could be leveraged to achieve superior tumour control. To investigate this, we simulated tumour growth under RT alone, IT alone, and RT-IT combination, using a representative treatment schedule as a proof of concept (RT: 10 fractions of 5 Gy, administered 7 days apart; IT: 300 ng/cm^3, given 30 days after the final RT fraction in the combination arm), in order to assess whether the two therapies act synergistically (Figure 5).

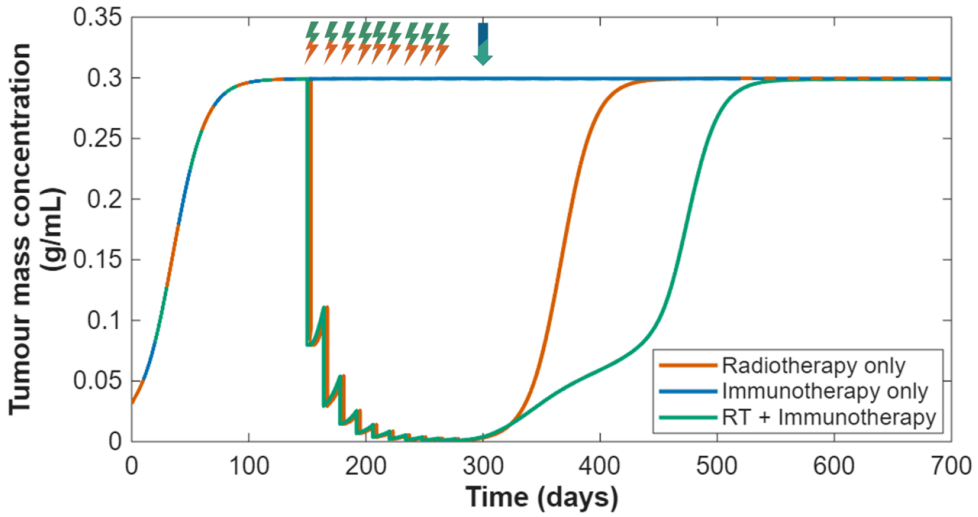

Figure 5 RT and anti-PD-L1 act synergistically against GBM. Tumour mass concentration over time is shown under radiotherapy alone, immunotherapy alone, and combined RT-IT treatment (10 fractions of 5 Gy, 14 days apart; anti-PD-L1 at 300 ng/mL, administered 30 days after the final RT fraction).

At the tested concentration, immunotherapy alone had negligible effect on tumour size, whereas radiotherapy alone achieved substantial tumour reduction during the treatment phase. However, under RT alone, the tumour relatively quickly returned to its pre-treatment dominant level, whereas in the combined RT-IT regimen, recurrence was markedly delayed. This suggests that RT provides an acute, immediate reduction in tumour burden, while IT delays the subsequent tumour recurrence, thus together offering proof-of-concept evidence of a synergistic interaction between the two therapies.

3.2 RT-IT Combination Treatments

Having established that RT-IT combinations may yield improved patient outcomes, we next sought to analyse how this synergistic benefit could be maximised by tuning the treatment schedule. A treatment schedule is characterised by several interacting factors including total radiation dose, number of fractions, dose per fraction, inter-fraction interval, immunotherapy dose, and the timing offset between radiotherapy and immunotherapy administration. Different combinations of these factors may yield markedly different synergistic outcomes. To evaluate how schedule design affects treatment efficacy, we defined three outcome measures by which each schedule is scored: time to progression, maximum tumour reduction, and tumour burden reduction. TTP measures the duration of tumour control following treatment before tumour relapses; MTR captures the maximum tumour shrinkage achieved; TBR quantifies the cumulative tumour burden avoided relative to no treatment, as the area between treated and untreated growth curves. The full mathematical formulation and derivation of these three outcome measures are provided in Appendix E.

The current standard of care (SOC) for GBM radiotherapy consists of a total dose of 60 Gy delivered in 30 daily fractions of 2 Gy over six weeks. In seeking improved treatment schedules without increasing damage to healthy tissue, we restrict our search to schedules that do not exceed this total radiation dose. To assess how the schedule characteristics described above (radiation dose, RT-IT timing offset, etc.) affect the chosen

outcome measures, we first fixed the immunotherapy concentration at 300 ng/cm^3 and evaluated 612 combinations of the remaining characteristics. Figure 6 presents the 196 most representative schedules, arranged as a heatmap matrix in which each row corresponds to a distinct outcome measure, and each cell within a column represents a single, unique treatment schedule.

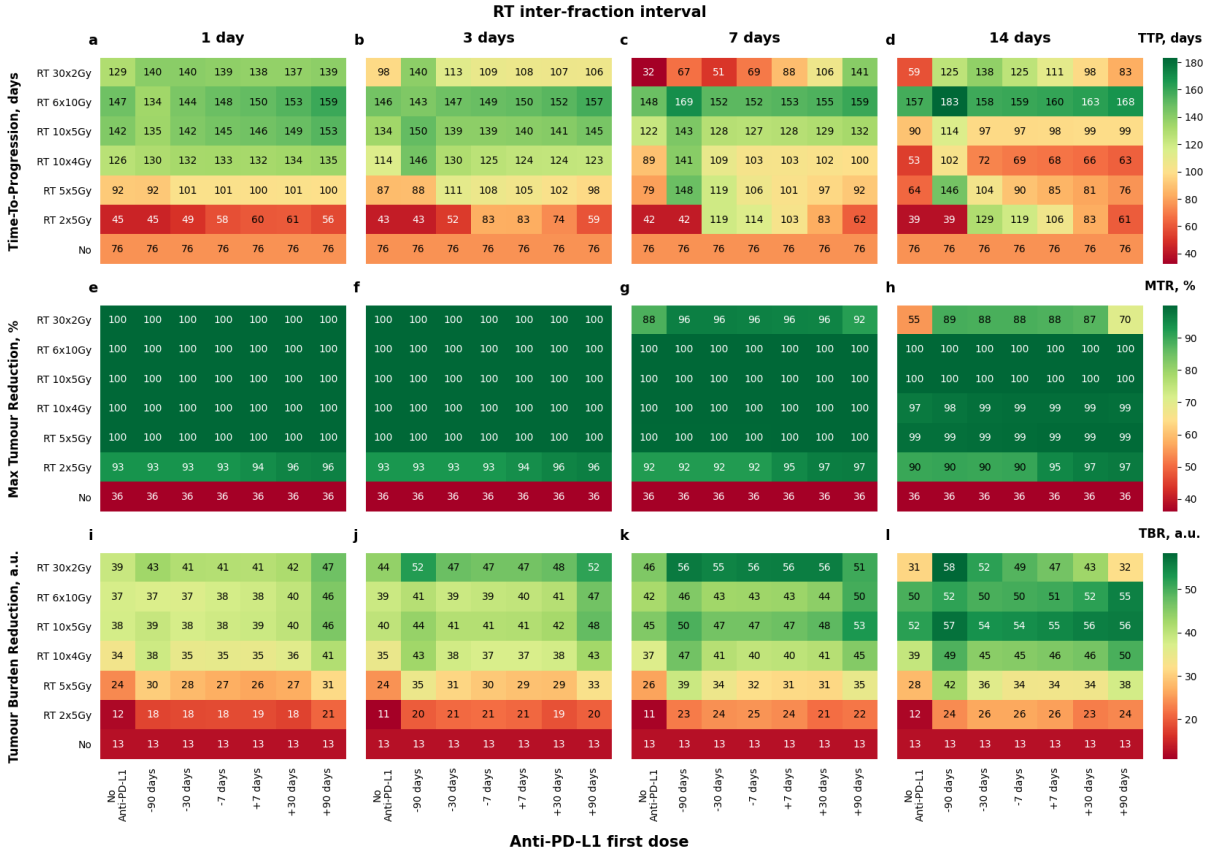

Figure 6 **a-d:** Time-to-progression (TTP, days), **e-h:** maximum tumour reduction (MTR, %), and **i-l:** tumour burden reduction (TBR, a.u.), for six RT fractionation schemes (rows) combined with anti-PD-L1 administered at varying times relative to the last/first RT fraction (columns), across four RT inter-fraction intervals (1, 3, 7, and 14 days). Negative values indicate that the last RT fraction is before administered anti-PD-L1; positive values indicate first RT fraction after anti-PD-L1 administration.

These results indicate that both RT fractionation and inter-fraction interval substantially influence TTP. To illustrate this, comparing the first row of the TTP heatmap (30×2 Gy - the SOC schedule, corresponding to the top-left cell of the 7-day interval column) with the second row (6×10 Gy) is instructive: despite delivering an identical total radiation dose, the two schedules yield markedly different TTP, with the 6×10 Gy regimen achieving superior tumour suppression. Notably, this difference is most pronounced at longer inter-fraction intervals, indicating that dose per fraction and inter-fraction timing interact rather than act independently. This is consistent with the underlying linear-quadratic radiobiological model, in which a larger dose per fraction requires sufficient time between fractions to fully exert its effect. This interaction is not monotonic, however: for the 10×4 Gy schedule, shorter inter-fraction intervals (1-3 days) yield longer TTP than longer intervals, the reverse of the pattern observed for 6×10 Gy. This confirms that the optimal inter-fraction interval is dose-dependent, rather than universally

longer being better, underscoring dose per fraction as a key determinant of the interval's effect. Immunotherapy timing also interacts with radiation dose: administering anti-PD-L1 after RT tends to improve outcomes, but this benefit is more pronounced at lower total radiation doses. At high doses, radiation's own effect dominates the response, diminishing the relative contribution of immunotherapy timing; at lower doses, however, immunotherapy scheduling becomes an important lever for achieving good outcomes while limiting a patient's total radiation exposure. This suggests that radiation-induced changes to the tumour microenvironment may open temporal windows during which checkpoint inhibition is particularly effective. Comparing TTP, MTR, and TBR reveals a further pattern: nearly all tested schedules achieve a high MTR (values reported as 100% in the figure are rounded and not exactly complete elimination), yet many perform poorly on TTP and TBR. This reinforces a defining feature of GBM treatment: the central therapeutic challenge is not achieving tumour reduction, which is comparatively easy, but suppressing relapse over time. TTP and TBR are therefore best interpreted together, as they capture complementary aspects of treatment response: TTP quantifies the duration of tumour control, while TBR captures the shape of the growth curve, specifically, how rapidly the tumour returns to its pre-treatment steady state once relapse begins.

To further examine how RT (particularly fractionation and dose per fraction) interacts with immunotherapy, and whether changing administered immunotherapy could help minimise administered radiation doses without significantly impairing outcomes, we analysed TTP across a range of immunotherapy concentrations and fraction numbers. Building on the previous results, we selected schedule settings that generally improved outcomes across the tested regimens: RT delivered with a 7-day inter-fraction interval, combined with immunotherapy administered 30 days after the final fraction. Using this fixed configuration, we then varied immunotherapy dose, number of fractions, and total RT dose. The results are presented as a heatmap in Figure 7.

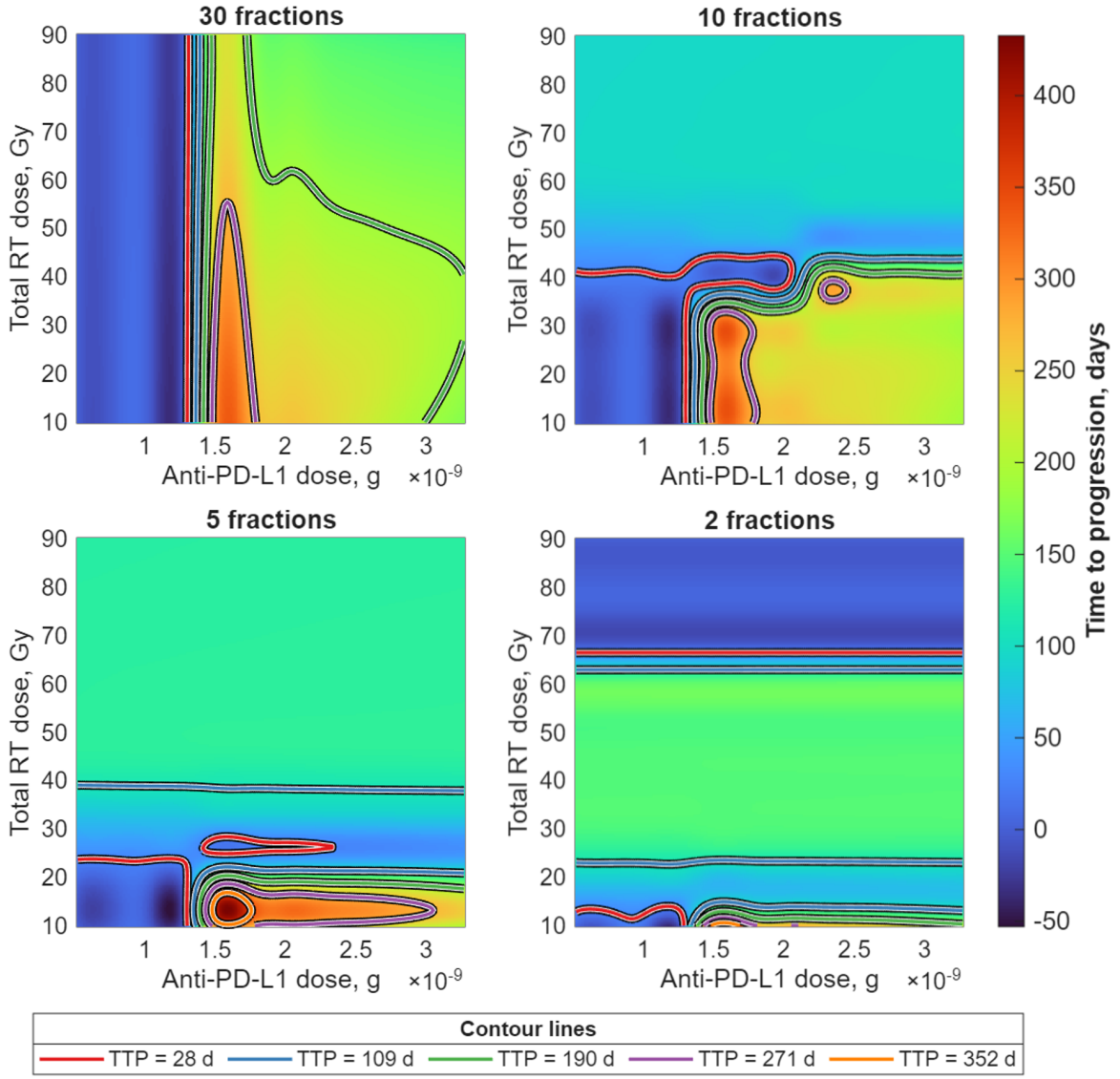

Figure 7 TTP depends on the interplay between RT dose and IT dose. Heatmaps show time-to-progression (TTP, days) as a function of total RT dose and anti-PD-L1 dose, for RT delivered across varying fraction counts, with immunotherapy administered at varying doses 30 days after the final RT fraction. Contour lines mark combinations of RT and anti-PD-L1 dose achieving equal TTP.

These results clearly demonstrate that specific combinations of RT and anti-PD-L1 dose define narrow windows of optimal treatment response, and that the relationship between the two is highly non-monotonic: increasing either dose in isolation does not necessarily improve TTP, and can in some cases worsen outcomes. A threshold-like anti-PD-L1 dose (approximately 1.4×10^{-9} g, or $\sim$21.4 ng/cm^3) is required before immunotherapy exerts a measurable positive effect, below which its contribution to TTP is negligible. Furthermore, comparing across the four fractionation regimes shows that a substantially lower total RT dose can achieve a comparable TTP when paired with an appropriately tuned number of fractions (and correspondingly, dose per fraction) and immunotherapy concentration, suggesting that healthy tissue exposure could potentially be reduced without compromising treatment efficacy.

3.3 Sensitivity Analysis and Simplified Model

Having established the model's dynamics under representative treatment scenarios, we next examined how variation in parameter values influences tumour-immune dynamics, in order to assess the robustness of our results and identify which parameters and compartments most strongly shape the observed dynamics of the GBM TME. For this purpose, we performed a global sensitivity analysis using Sobol indices [**sobol2001global**], which decompose the variance of a model output into contributions attributable to individual parameters' interactions with other parameters (called total-order indices), thereby identifying which parameters most strongly drive variation in model output.

Total tumour mass was taken as the reference output, evaluated under a reference treatment schedule consisting of a single 5 Gy radiotherapy dose administered 50 days after the tumour reached steady state, combined with immunotherapy at 300 ng/cm^3 administered 7 days after RT (time $t = 0$ is defined as the day the tumour first reaches steady state). Parameters drawn from the literature were varied within a narrower range (0.5×–1.5× their nominal value), reflecting greater confidence in these estimates, while parameters obtained through model-based estimation were varied across two orders of magnitude (0.1×–10×), reflecting their comparatively higher uncertainty. Following convention in the sensitivity analysis literature [39], a Sobol index of 0.1 was taken as the threshold for a parameter to be considered a significant contributor to output variance. Sobol indices were computed both before and after administration of the RT-IT combination, allowing us to assess whether parameter influence shifts under treatment. Figure 8 reports only those parameters that exceeded this threshold at either timepoint, out of the full set of model parameters tested.

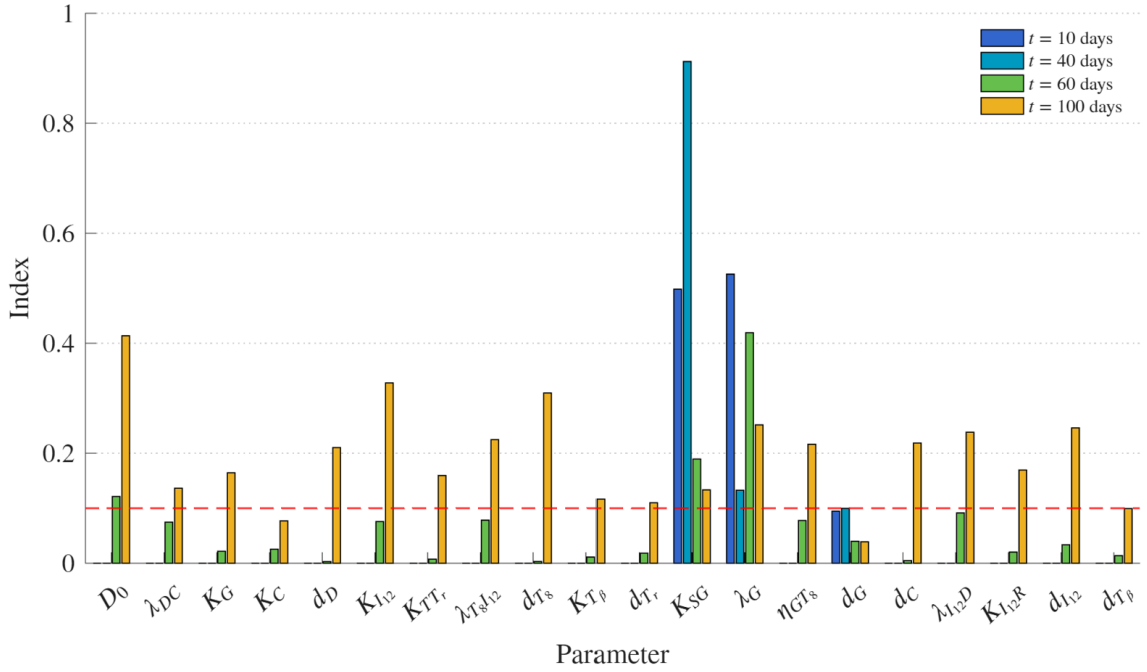

Figure 8 Global Sensitivity Analysis. Sobol sensitivity indices for total tumour mass, shown at four timepoints spanning the pre- and post-treatment period ($t = 10$ and 40 days, before RT-IT administration; $t = 60$ and 100 days, after). Only parameters exceeding the significance threshold (Sobol index > 0.1, dashed red line) at any timepoint are shown, out of the full set of model parameters tested.

The analysis reveals that, although treatment administration increases the overall variance attributable to model parameters, the set of parameters with a significant effect on tumour size variance remains limited, consisting predominantly of parameters associated with dendritic cells, $CD8^+$ T cells, and IL-12. This indicates that the remaining parameters, including several of those estimated within this study, can reasonably be treated as fixed, since variation within their tested ranges produced no significant change in model output. Consequently, several compartments contribute negligibly to the model's overall behaviour, motivating a simplification of the model structure. Guided by the key dynamics identified in Figures 2-4, we constructed a reduced model comprising bulk tumour cells, glioma stem cells (retained to capture GBM's characteristic therapy resistance and relapse), dendritic cells, $CD8^+$ T cells, IL-12, as well as PD-1 and PD-L1. This simplified model is shown in Figure 9.

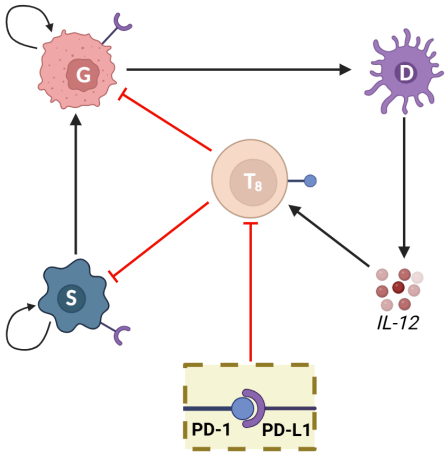

Figure 9 Simplified model schematic. Sharp arrows indicate proliferation/activation; blocked arrows indicate killing/inhibition. G: differentiated cancer cells; S: glioma stem cells; D: dendritic cells; T8: CD8+ T cells; T8 cells express PD-1, G,S cells express PD-L1.

The proposed simplified model offers a valuable tool for future studies of GBM TME dynamics, as well as for clinical applications. Its reduced complexity makes it more tractable and interpretable than the full model, while still effectively capturing tumour progression dynamics and treatment response to combination therapies. As such, it is well suited to accommodating patient-specific cases and scenarios, providing information to support treatment-planning decisions.

4 Conclusions and limitations

Glioblastoma (GBM) is among the most common and aggressive primary brain cancers, remaining highly resistant to conventional therapies, including radiotherapy (RT), due to the dynamic and adaptive nature of its tumour microenvironment (TME). With the emergence of immunotherapy as a promising avenue in GBM treatment, a compelling rationale has developed for combining RT with anti-PD-L1 checkpoint inhibition. However, how best to schedule and dose such combinations to maximise clinical benefit remained poorly understood.

In this work, we developed a mathematical model, formulated as a system of ordinary differential equations, describing the cellular and cytokine cross-talk within the GBM TME. We first characterised tumour and microenvironment dynamics by comparing model simulations in the absence and presence of therapy, providing computational evidence that RT and anti-PD-L1 act synergistically to improve tumour control. Building on this, we compared a range of treatment schedules to assess how key factors influence patient outcomes. This revealed a complex, non-monotonic relationship between RT-IT scheduling and treatment response, with dose per fraction and its interaction with inter-fraction spacing emerging as a particularly influential factor. We further found that administering immunotherapy after RT generally improves outcomes, likely by exploiting radiation-induced changes in the TME. By jointly varying fractionation and immunotherapy dose, we identified schedules that reduce total radiation dose and thus damage to healthy tissue, while preserving treatment efficacy. This yielded candidate schedules with substantial improvements over current standard of care that could inform future clinical trial design. Finally, a global parameter sensitivity analysis identified the TME components with the greatest influence on model outcomes, motivating a simplified reduced-order model suited to clinical use in developing patient-specific treatment schedules.

While the proposed model offers valuable insight into optimising GBM treatment through RT-IT combination, several limitations of its TME representation should be acknowledged:

1. **Absence of spatial heterogeneity.** As a system of ODEs, the model captures only temporal dynamics, assuming a spatially homogeneous TME and constant tumour volume. Spatial factors, such as tumour heterogeneity and chemotactic gradients, are known to significantly shape tumour-immune interactions in GBM. While incorporating spatial structure would substantially increase model complexity and reduce interpretability, its absence here limits the model's direct applicability to real-world clinical scenarios.

2. **Absence of metabolic and nutritional factors.** Nutrient availability and the broader metabolic environment, including glucose availability, hypoxia, and acidosis, are known to substantially impair immune function and shape tumour-immune dynamics, but are not captured by the current model.

In conclusion, the developed model provides valuable insight into the GBM TME and into strategies for optimising patient outcomes through combined RT-IT treatment, identifying schedules with the potential to meaningfully outperform current standards of care. These findings offer a rational basis for future clinical trial design, as well as providing a practical tool for supporting patient-specific treatment-planning decisions.

References

[1] Radu Albulescu et al. "Cytokine Patterns in Brain Tumour Progression". In: *Mediators of Inflammation* 2013 (2013), pp. 1–7. DOI: 10.1155/2013/979748.

[2] "An elementary approach to modeling drug resistance in cancer". In: *Mathematical Biosciences and Engineering* 7.4 (2010), pp. 905–918. DOI: 10.3934/mbe.2010.7.905.

[3] Abul Azad et al. "PD-L1 blockade enhances response of pancreatic ductal adenocarcinoma to radiotherapy". In: *EMBO Molecular Medicine* 9.2 (2016), pp. 167–180. DOI: 10.15252/emmm.201606674.

[4] Sandip Banerjee, Subhas Khajanchi, and Swapna Chaudhuri. "A Mathematical Model to Elucidate Brain Tumor Abrogation by Immunotherapy with T11 Target Structure". In: *PLOS ONE* 10.5 (2015), e0123611. DOI: 10.1371/journal.pone.0123611.

[5] Jill S. Barnholtz-Sloan, Quinn T. Ostrom, and David Cote. "Epidemiology of Brain Tumors". In: *Neurologic Clinics* 36.3 (2018), pp. 395–419. DOI: 10.1016/j.ncl.2018.04.001.

[6] Rebecca Anne Bekker et al. "Mathematical modeling of radiotherapy and its impact on tumor interactions with the immune system". In: *Neoplasia* 28 (2022), p. 100796. DOI: 10.1016/j.neo.2022.100796.

[7] Yuanzhi Bian, Debra L. Walter, and Chenming Zhang. "Efficiency of Interferon- in Activating Dendritic Cells and Its Potential Synergy with Toll-like Receptor Agonists". In: *Viruses* 15.5 (2023), p. 1198. DOI: 10.3390/v15051198.

[8] Christine E. Brown et al. "Recognition and Killing of Brain Tumor Stem-Like Initiating Cells by CD8+ Cytolytic T Cells". In: *Cancer Research* 69.23 (2009), pp. 8886–8893. DOI: 10.1158/0008-5472.can-09-2687.

[9] Krystal R Charley et al. "Effector-Phase IL-2 Signals Drive Th1 Effector and Memory Responses Dependently and Independently of TCF-1". In: *The Journal of Immunology* 212.4 (2023), pp. 586–595. DOI: 10.4049/jimmunol.2300570.

[10] Jianan Chen et al. "Tumor-Associated Macrophages in Glioblastoma: Mechanisms of Tumor Progression and Therapeutic Strategies". In: *Cells* 14.18 (2025), p. 1458. DOI: 10.3390/cells14181458.

[11] Shanze Chen et al. "Macrophages in immunoregulation and therapeutics". In: *Signal Transduction and Targeted Therapy* 8.1 (2023). DOI: 10.1038/s41392-023-01452-1.

[12] W. Chen and J. E. Konkel. "TGF- and 'Adaptive' Foxp3+ Regulatory T cells". In: *Journal of Molecular Cell Biology* 2.1 (2009), pp. 30–36. DOI: 10.1093/jmcb/mjp004.

[13] Zhihong Chen et al. "A paracrine circuit of IL-1/IL-1R1 between myeloid and tumor cells drives genotype-dependent glioblastoma progression". In: *Journal of Clinical Investigation* 133.22 (2023). DOI: 10.1172/jci163802.

[14] Marius Ciurea et al. "Cancer Stem Cells: Biological Functions and Therapeutically Targeting". In: *International Journal of Molecular Sciences* 15.5 (2014), pp. 8169–8185. DOI: 10.3390/ijms15058169.

[15] Chloé Colson et al. "Mathematical modelling of cancer cell evolution and plasticity". In: *Current Opinion in Cell Biology* 95 (2025), p. 102558. DOI: 10.1016/j.ceb.2025.102558.

[16] James F Curtin et al. "HMGB1 Mediates Endogenous TLR2 Activation and Brain Tumor Regression". In: *PLoS Medicine* 6.1 (2009), e1000010. DOI: 10.1371/journal.pmed.1000010.

[17] Bożena Czarkowska-Paczek, I Bartłomiejczyk, and Jacek Przybylski. "The serum levels of growth factors: PDGF, TGF-beta and VEGF are increased after strenuous physical exercise." In: *PubMed* 57.2 (2006), pp. 189–97.

[18] Judy Day, Avner Friedman, and Larry S. Schlesinger. "Modeling the immune rheostat of macrophages in the lung in response to infection". In: *Proceedings of the National Academy of Sciences* 106.27 (2009), pp. 11246–11251. DOI: 10.1073/pnas.0904846106.

[19] Roxana Deleanu, Laura Cristina Ceafalan, and Anica Dricu. "Transcriptomic Crosstalk between Gliomas and Telencephalic Neural Stem and Progenitor Cells for Defining Heterogeneity and Targeted Signaling Pathways". In: *International Journal of Molecular Sciences* 22.24 (2021), p. 13211. DOI: 10.3390/ijms222413211.

[20] Anja Derer et al. "Chemoradiation Increases PD-L1 Expression in Certain Melanoma and Glioblastoma Cells". In: *Frontiers in Immunology* 7 (2016). DOI: 10.3389/fimmu.2016.00610.

[21] Anna Maria Di Giacomo et al. "Immunotherapy of brain metastases: breaking a "dogma"". In: *Journal of Experimental & Clinical Cancer Research* 38.1 (2019). DOI: 10.1186/s13046-019-1426-2.

[22] Tarekegn Dinku et al. "A Mathematical Model of Tumor-Immune and Host Cells Interactions with Chemotherapy and Optimal Control". In: *Journal of Mathematics* 2024.1 (2024). DOI: 10.1155/2024/3395825.

[23] Simon J. Dovedi et al. "Acquired Resistance to Fractionated Radiotherapy Can Be Overcome by Concurrent PD-L1 Blockade". In: *Cancer Research* 74.19 (2014), pp. 5458–5468. DOI: 10.1158/0008-5472.can-14-1258.

[24] Ilker Y. Eyüpoglu, Michael Buchfelder, and Nic E. Savaskan. "Surgical resection of malignant gliomas—role in optimizing patient outcome". In: *Nature Reviews Neurology* 9.3 (2013), pp. 141–151. DOI: 10.1038/nrneurol.2012.279.

[25] Jacopo Falco et al. "In Silico Mathematical Modelling for Glioblastoma: A Critical Review and a Patient-Specific Case". In: *Journal of Clinical Medicine* 10.10 (2021), p. 2169. DOI: 10.3390/jcm10102169.

[26] Loise M. Francisco et al. "PD-L1 regulates the development, maintenance, and function of induced regulatory T cells". In: *Journal of Experimental Medicine* 206.13 (2009), pp. 3015–3029. DOI: 10.1084/jem.20090847.

[27] Avner Friedman and Wenrui Hao. "The Role of Exosomes in Pancreatic Cancer Microenvironment". In: *Bulletin of Mathematical Biology* 80.5 (2017), pp. 1111–1133. DOI: 10.1007/s11538-017-0254-9.

[28] Sofia R. Gameiro et al. "Radiation-induced immunogenic modulation of tumor enhances antigen processing and calreticulin exposure, resulting in enhanced T-cell killing". In: *Oncotarget* 5.2 (2013), pp. 403–416. DOI: 10.18632/oncotarget.1719.

[29] Xuefeng Gao et al. "Acute and Fractionated Irradiation Differentially Modulate Glioma Stem Cell Division Kinetics". In: *Cancer Research* 73.5 (2012), pp. 1481–1490. DOI: 10.1158/0008-5472.can-12-3429.

[30] L M Garcia et al. "Fitting the linear–quadratic model to detailed data sets for different dose ranges". In: *Physics in Medicine and Biology* 51.11 (2006), pp. 2813–2823. DOI: 10.1088/0031-9155/51/11/009.

[31] Sara N. Gentry and Trachette L. Jackson. "A Mathematical Model of Cancer Stem Cell Driven Tumor Initiation: Implications of Niche Size and Loss of Homeostatic Regulatory Mechanisms". In: *PLoS ONE* 8.8 (2013), e71128. DOI: 10.1371/journal.pone.0071128.

[32] Amina Ghouzlani et al. "Immune Checkpoint Inhibitors in Human Glioma Microenvironment". In: *Frontiers in Immunology* 12 (2021). DOI: 10.3389/fimmu.2021.679425.

[33] S. Gu et al. "Applying a patient-specific bio-mathematical model of glioma growth to develop virtual [18F]-FMISO-PET images". In: *Mathematical Medicine and Biology* 29.1 (2011), pp. 31–48. DOI: 10.1093/imammb/dqr002.

[34] Therwa Hamza, John B. Barnett, and Bingyun Li. "Interleukin 12 a Key Immunoregulatory Cytokine in Infection Applications". In: *International Journal of Molecular Sciences* 11.3 (2010), pp. 789–806. DOI: 10.3390/ijms11030789.

[35] Chengcheng Hao et al. "PD-L1 Expression in Glioblastoma, the Clinical and Prognostic Significance: A Systematic Literature Review and Meta-Analysis". In: *Frontiers in Oncology* 10 (2020). DOI: 10.3389/fonc.2020.01015.

[36] Wenrui Hao, Elliott D. Crouser, and Avner Friedman. "Mathematical model of sarcoidosis". In: *Proceedings of the National Academy of Sciences* 111.45 (2014), pp. 16065–16070. DOI: 10.1073/pnas.1417789111.

[37] Wenrui Hao and Avner Friedman. "Mathematical model on Alzheimer's disease". In: *BMC Systems Biology* 10.1 (2016). DOI: 10.1186/s12918-016-0348-2.

[38] Elvin't Hart et al. "Blood-brain barrier permeability following conventional photon radiotherapy – A systematic review and meta-analysis of clinical and preclinical studies". In: *Clinical and Translational Radiation Oncology* 35 (2022), pp. 44–55. DOI: 10.1016/j.ctro.2022.04.013.

[39] J. D. Herman et al. "Technical Note: Method of Morris effectively reduces the computational demands of global sensitivity analysis for distributed watershed models". In: *Hydrology and Earth System Sciences* 17.7 (2013), pp. 2893–2903. DOI: 10.5194/hess-17-2893-2013.

[40] Lan B. Hoang-Minh and Duane A. Mitchell. "Immunotherapy for Brain Tumors". In: *Current Treatment Options in Oncology* 19.11 (2018). DOI: 10.1007/s11864-018-0576-3.

[41] David A. Hormuth et al. "Opportunities for improving brain cancer treatment outcomes through imaging-based mathematical modeling of the delivery of radiotherapy and immunotherapy". In: *Advanced Drug Delivery Reviews* 187 (2022), p. 114367. DOI: 10.1016/j.addr.2022.114367.

[42] Saket Jain et al. "Single-cell RNA sequencing and spatial transcriptomics reveal cancer-associated fibroblasts in glioblastoma with protumoral effects". In: *Journal of Clinical Investigation* 133.5 (2023). DOI: 10.1172/jci147087.

[43] Pawel Jarmuzek et al. "Cytokine Profile in Development of Glioblastoma in Relation to Healthy Individuals". In: *International Journal of Molecular Sciences* 24.22 (2023), p. 16206. DOI: 10.3390/ijms242216206.

[44] Baowei Ji et al. "Glioma Stem Cell-Targeted Dendritic Cells as a Tumor Vaccine Against Malignant Glioma". In: *Yonsei Medical Journal* 54.1 (2013), p. 92. DOI: 10.3349/ymj.2013.54.1.92.

[45] Keaton I Jones et al. "Radiation combined with macrophage depletion promotes adaptive immunity and potentiates checkpoint blockade". In: *EMBO Molecular Medicine* 10.12 (2018). DOI: 10.15252/emmm.201809342.

[46] Bozena Kaminska, Aleksandra Wesolowska, and Malgorzata Danilkiewicz. "TGF beta signalling and its role in tumour pathogenesis." In: *Acta Biochimica Polonica* 52.2 (2005), pp. 329–337. DOI: 10.18388/abp.2005_3446.

[47] Punit Kaur and Alexzander Asea. "Radiation-induced effects and the immune system in cancer". In: *Frontiers in Oncology* 2 (2012). DOI: 10.3389/fonc.2012.00191.

[48] Choong-Hyun Koh et al. "CD8 T-cell subsets: heterogeneity, functions, and therapeutic potential". In: *Experimental & Molecular Medicine* 55.11 (2023), pp. 2287–2299. DOI: 10.1038/s12276-023-01105-x.

[49] S Krüger-Krasagakes et al. "Expression of interleukin 10 in human melanoma". In: *British Journal of Cancer* 70.6 (1994), pp. 1182–1185. DOI: 10.1038/bjc.1994.469.

[50] Yo-Ping Lai et al. "CD4+ T Cell-Derived IL-2 Signals during Early Priming Advances Primary CD8+ T Cell Responses". In: *PLoS ONE* 4.11 (2009), e7766. DOI: 10.1371/journal.pone.0007766.

[51] Xiulan Lai and Avner Friedman. "Mathematical modeling of cancer treatment with radiation and PD-L1 inhibitor". In: *Science China Mathematics* 63.3 (2020), pp. 465–484. DOI: 10.1007/s11425-019-1648-6.

[52] Xiulan Lai, Wenrui Hao, and Avner Friedman. "TNF- inhibitor reduces drug-resistance to anti-PD-1: A mathematical model". In: *PLOS ONE* 15.4 (2020), e0231499. DOI: 10.1371/journal.pone.0231499.

[53] Xiulan Lai et al. "Modeling combination therapy for breast cancer with BET and immune checkpoint inhibitors". In: *Proceedings of the National Academy of Sciences* 115.21 (2018), pp. 5534–5539. DOI: 10.1073/pnas.1721559115.

[54] Francesco Lasorsa et al. “Immune Checkpoint Inhibitors in Renal Cell Carcinoma: Molecular Basis and Rationale for Their Use in Clinical Practice”. In: *Biomedicines* 11.4 (2023), p. 1071. DOI: 10.3390/biomedicines11041071.

[55] Eun-Jung Lee et al. “Radiation Inhibits Interleukin-12 Production via Inhibition of C-Rel through the Interleukin-6/ Signal Transducer and Activator of Transcription 3 Signaling Pathway in Dendritic Cells”. In: *PLOS ONE* 11.1 (2016), e0146463. DOI: 10.1371/journal.pone.0146463.

[56] Stewart Leung et al. “The cytokine milieu in the interplay of pathogenic Th1/Th17 cells and regulatory T cells in autoimmune disease”. In: *Cellular & Molecular Immunology* 7.3 (2010), pp. 182–189. DOI: 10.1038/cmi.2010.22.

[57] Heng-Hong Li et al. “Ionizing Radiation Impairs T Cell Activation by Affecting Metabolic Reprogramming”. In: *International Journal of Biological Sciences* 11.7 (2015), pp. 726–736. DOI: 10.7150/ijbs.12009.

[58] Nannan Li et al. “Armored bicistronic CAR T cells with dominant-negative TGF- receptor II to overcome resistance in glioblastoma”. In: *Molecular Therapy* 32.10 (2024), pp. 3522–3538. DOI: 10.1016/j.ymthe.2024.07.020.

[59] Wei Liao, Jian-Xin Lin, and Warren J Leonard. “IL-2 family cytokines: new insights into the complex roles of IL-2 as a broad regulator of T helper cell differentiation”. In: *Current Opinion in Immunology* 23.5 (2011), pp. 598–604. DOI: 10.1016/j.coi.2011.08.003.

[60] E. Liniker et al. “Activity and safety of radiotherapy with anti-PD-1 drug therapy in patients with metastatic melanoma”. In: *OncoImmunology* 5.9 (2016), e1214788. DOI: 10.1080/2162402x.2016.1214788.

[61] Jialing Liu et al. “TGF- in tumor development and progression: mechanisms and therapeutics”. In: *Molecular Biomedicine* 7.1 (2026). DOI: 10.1186/s43556-026-00403-w.

[62] Shasha Liu et al. “Regulatory T cells promote glioma cell stemness through TGF-–NF-B–IL6–STAT3 signaling”. In: *Cancer Immunology, Immunotherapy* 70.9 (2021), pp. 2601–2616. DOI: 10.1007/s00262-021-02872-0.

[63] Zhengzheng Liu et al. “TGF-1 secreted by M2 phenotype macrophages enhances the stemness and migration of gliomacells via the SMAD2/3 signalling pathway”. In: *International Journal of Molecular Medicine* (2018). DOI: 10.3892/ijmm.2018.3923.

[64] Wing-Cheong Lo et al. “Inflammatory Bowel Disease: How Effective Is TNF- Suppression?” In: *PLOS ONE* 11.11 (2016), e0165782. DOI: 10.1371/journal.pone.0165782.

[65] Devin M. Lonergan et al. “Growth Factor Profile of Irradiated Human Dermal Fibroblasts Using a Serum-Free Method”. In: *Plastic and Reconstructive Surgery* 111.6 (2003), pp. 1960–1968. DOI: 10.1097/01.prs.0000055065.41599.75.

[66] Gloria Lopez-Castejon and David Brough. “Understanding the mechanism of IL-1 secretion”. In: *Cytokine & Growth Factor Reviews* 22.4 (2011), pp. 189–195. DOI: 10.1016/j.cytogfr.2011.10.001.

[67] Min Luo et al. “Macrophage polarization: an important role in inflammatory diseases”. In: *Frontiers in Immunology* 15 (2024). DOI: 10.3389/fimmu.2024.1352946.

[68] Shreya Maiti et al. “Mathematical Modeling of Pro- and Anti-Inflammatory Signaling in Macrophages”. In: *Processes* 3.1 (2014), pp. 1–18. DOI: 10.3390/pr3010001.

[69] Perla Marmolejo-León et al. “Estimation of the effectiveness ratio (/) for resistant cancer cells in U87MG human glioblastoma”. In: *Applied Radiation and Isotopes* 141 (2018), pp. 156–161. DOI: 10.1016/j.apradiso.2018.01.011.

[70] Roy L. Maute et al. “Engineering high-affinity PD-1 variants for optimized immunotherapy and immuno-PET imaging”. In: *Proceedings of the National Academy of Sciences* 112.47 (2015). DOI: 10.1073/pnas.1519623112.

[71] Maxime Meylan et al. “Persistent T cell activation and cytotoxicity against glioblastoma following single oncolytic virus treatment in a clinical trial”. In: *Cell* 189.5 (2026), 1287–1304.e18. DOI: 10.1016/j.cell.2025.12.055.

[72] Keyhan Minaee et al. “57: EVALUATION OF THE CIRCULATING LEVELS OF IL-12 AND IL-33 IN PATIENTS WITH BREAST CANCER: INFLUENCES OF THE TUMOR STAGES AND CYTOKINE GENE POLYMORPHISMS”. In: *BMJ Open* 7.Suppl 1 (2017), bmjopen–2016-015415.57. DOI: 10.1136/bmjopen-2016-015415.57.

[73] Erin Morrow et al. “Production of Proinflammatory Cytokines by CD4+ and CD8+ T Cells in Response to Mycobacterial Antigens among Children and Adults with Tuberculosis”. In: *Pathogens* 12.11 (2023), p. 1353. DOI: 10.3390/pathogens12111353.

[74] Domenique M J Müller et al. “Timing of glioblastoma surgery and patient outcomes: a multicenter cohort study”. In: *Neuro-Oncology Advances* 3.1 (2021). DOI: 10.1093/noajnl/vdab053.

[75] Patricia Ngai et al. “Gamma Interferon Responses of CD4 and CD8 T-Cell Subsets Are Quantitatively Different and Independent of Each Other during Pulmonary Mycobacterium bovis BCG Infection”. In: *Infection and Immunity* 75.5 (2007), pp. 2244–2252. DOI: 10.1128/iai.00024-07.

[76] Antonio Omuro. “Glioblastoma and Other Malignant Gliomas”. In: *JAMA* 310.17 (2013), p. 1842. DOI: 10.1001/jama.2013.280319.

[77] Q. T. Ostrom et al. “CBTRUS Statistical Report: Primary Brain and Central Nervous System Tumors Diagnosed in the United States in 2006-2010”. In: *Neuro-Oncology* 15.suppl 2 (2013), pp. ii1–ii56. DOI: 10.1093/neuonc/not151.

[78] Quinn T Ostrom et al. “CBTRUS Statistical Report: Primary Brain and Other Central Nervous System Tumors Diagnosed in the United States in 2013–2017”. In: *Neuro-Oncology* 22.Supplement$_1$ (2020), pp. iv1–iv96. DOI: 10.1093/neuonc/noaa200.

[79] Harald Paganetti. “A review on lymphocyte radiosensitivity and its impact on radiotherapy”. In: *Frontiers in Oncology* 13 (2023). DOI: 10.3389/fonc.2023.1201500.

[80] Jianping Pan et al. “Interferon- is an autocrine mediator for dendritic cell maturation”. In: *Immunology Letters* 94.1-2 (2004), pp. 141–151. DOI: 10.1016/j.imlet.2004.05.003.

[81] Changming Pang and Yan Wang. “The Immunosuppressive Microenvironment of Glioblastoma: Mechanisms, Clinical Challenges and Future Directions”. In: *Immunology* 177.4 (2025), pp. 662–673. DOI: 10.1111/imm.70087.

[82] Carole Yolande Perrot, Delphine Javelaud, and Alain Mauviel. “Insights into the Transforming Growth Factor-Signaling Pathway in Cutaneous Melanoma”. In: *Annals of Dermatology* 25.2 (2013), p. 135. DOI: 10.5021/ad.2013.25.2.135.

[83] Rifaquat Rahman et al. “DNA damage response in brain tumors: A Society for Neuro-Oncology consensus review on mechanisms and translational efforts in neuro-oncology”. In: *Neuro-Oncology* 26.8 (2024), pp. 1367–1387. DOI: 10.1093/neuonc/noae072.

[84] Silvia Mara Baez Rodriguez et al. “Glioblastoma Stem Cells—Useful Tools in the Battle against Cancer”. In: *International Journal of Molecular Sciences* 23.9 (2022), p. 4602. DOI: 10.3390/ijms23094602.

[85] R.K. Sachs, L.R. Hlatky, and P. Hahnfeldt. “Simple ODE models of tumor growth and anti-angiogenic or radiation treatment”. In: *Mathematical and Computer Modelling* 33.12-13 (2001), pp. 1297–1305. DOI: 10.1016/s0895-7177(00)00316-2.

[86] Li Shi et al. “The role of PD-1 and PD-L1 in T-cell immune suppression in patients with hematological malignancies”. In: *Journal of Hematology & Oncology* 6.1 (2013). DOI: 10.1186/1756-8722-6-74.

[87] Tsutomu Shimura et al. “Radiation-Induced Myofibroblasts Promote Tumor Growth via Mitochondrial ROS–Activated TGF Signaling”. In: *Molecular Cancer Research* 16.11 (2018), pp. 1676–1686. DOI: 10.1158/1541-7786.mcr-18-0321.

[88] Fatemeh Shiridokht et al. “Advancing cancer radiotherapy: Harnessing radiosensitizers and nanotechnology for enhanced tumor control”. In: *International Journal of Pharmaceutics: X* 10 (2025), p. 100419. DOI: 10.1016/j.ijpx.2025.100419.

[89] Dhruv Sud et al. “Contribution of CD8+ T Cells to Control of Mycobacterium tuberculosis Infection”. In: *The Journal of Immunology* 176.7 (2006), pp. 4296–4314. DOI: 10.4049/jimmunol.176.7.4296.

[90] K. R. Swanson, E. C. Alvord, and J. D. Murray. “A quantitative model for differential motility of gliomas in grey and white matter”. In: *Cell Proliferation* 33.5 (2000), pp. 317–329. DOI: 10.1046/j.1365-2184.2000.00177.x.

[91] Qing Tang et al. “The role of PD-1/PD-L1 and application of immune-checkpoint inhibitors in human cancers”. In: *Frontiers in Immunology* 13 (2022). DOI: 10.3389/fimmu.2022.964442.

[92] Feifei Teng et al. “Radiotherapy combined with immune checkpoint blockade immunotherapy: Achievements and challenges”. In: *Cancer Letters* 365.1 (2015), pp. 23–29. DOI: 10.1016/j.canlet.2015.05.012.

[93] Ana Teresa Pinto et al. “Ionizing radiation modulates human macrophages towards a pro-inflammatory phenotype preserving their pro-invasive and pro-angiogenic capacities”. In: *Scientific Reports* 6.1 (2016). DOI: 10.1038/srep18765.

[94] Yosuke Togashi, Kohei Shitara, and Hiroyoshi Nishikawa. “Regulatory T cells in cancer immunosuppression — implications for anticancer therapy”. In: *Nature Reviews Clinical Oncology* 16.6 (2019), pp. 356–371. DOI: 10.1038/s41571-019-0175-7.

[95] Cristian Tomasetti and Doron Levy. “Role of symmetric and asymmetric division of stem cells in developing drug resistance”. In: *Proceedings of the National Academy of Sciences* 107.39 (2010), pp. 16766–16771. DOI: 10.1073/pnas.1007726107.

[96] Rut Valdor et al. “Glioblastoma progression is assisted by induction of immunosuppressive function of pericytes through interaction with tumor cells”. In: *Oncotarget* 8.40 (2017), pp. 68614–68626. DOI: 10.18632/oncotarget.19804.

[97] Marco van Vulpen et al. “Changes in blood-brain barrier permeability induced by radiotherapy: Implications for timing of chemotherapy? (Review)”. In: *Oncology Reports* (2002). DOI: 10.3892/or.9.4.683.

[98] Jiguang Wang et al. “Clonal evolution of glioblastoma under therapy”. In: *Nature Genetics* 48.7 (2016), pp. 768–776. DOI: 10.1038/ng.3590.

[99] Lei Wang et al. “Interleukin-1 and transforming growth factor- cooperate to induce neurosphere formation and increase tumorigenicity of adherent LN-229 glioma cells”. In: *Stem Cell Research & Therapy* 3.1 (2012). DOI: 10.1186/scrt96.

[100] Weimin Wang et al. “CD8+ T Cells in Immunotherapy, Radiotherapy, and Chemotherapy”. In: *Oncoimmunology*. Springer International Publishing, 2017, pp. 23–39. DOI: 10.1007/978-3-319-62431-0_3.

[101] Michael Weller et al. “EANO guidelines on the diagnosis and treatment of diffuse gliomas of adulthood”. In: *Nature Reviews Clinical Oncology* 18.3 (2020), pp. 170–186. DOI: 10.1038/s41571-020-00447-z.

[102] Gavin Whitehouse et al. “IL-2 therapy restores regulatory T-cell dysfunction induced by calcineurin inhibitors”. In: *Proceedings of the National Academy of Sciences* 114.27 (2017), pp. 7083–7088. DOI: 10.1073/pnas.1620835114.

[103] Adam Wu et al. “Glioma cancer stem cells induce immunosuppressive macrophages/microglia”. In: *Neuro-Oncology* 12.11 (2010), pp. 1113–1125. DOI: 10.1093/neuonc/noq082.

[104] Huaming Yan et al. “3D Mathematical Modeling of Glioblastoma Suggests That Transdifferentiated Vascular Endothelial Cells Mediate Resistance to Current Standard-of-Care Therapy”. In: *Cancer Research* 77.15 (2017), pp. 4171–4184. DOI: 10.1158/0008-5472.can-16-3094.

[105] Raymund L. Yong and Russell R. Lonser. "Surgery for Glioblastoma Multiforme: Striking a Balance". In: *World Neurosurgery* 76.6 (2011), pp. 528–530. DOI: 10.1016/j.wneu.2011.06.053.

[106] Xin Yong et al. "Regulation of the CD8 T cell and PDL1/PD1 axis in gastric cancer: Unraveling the molecular landscape". In: *Critical Reviews in Oncology/Hematology* 212 (2025), p. 104750. DOI: 10.1016/j.critrevonc.2025.104750.

[107] Kristina H. Young et al. "Optimizing Timing of Immunotherapy Improves Control of Tumors by Hypofractionated Radiation Therapy". In: *PLOS ONE* 11.6 (2016), e0157164. DOI: 10.1371/journal.pone.0157164.

[108] Xianlin Zeng et al. "High-dose radiation induces dendritic cells maturation by promoting immunogenic cell death in nasopharyngeal carcinoma". In: *Frontiers in Immunology* 16 (2025). DOI: 10.3389/fimmu.2025.1554018.

[109] Zixin Zhang et al. "Mathematical model of tumor immune microenvironment with application to the combined therapy targeting the PD-1/PD-L1 pathway and IL-10 cytokine antibody". In: *Theory in Biosciences* 144.1 (2024), pp. 19–43. DOI: 10.1007/s12064-024-00428-1.

[110] Tiancheng Zhao et al. "PD-L1 expression increased by IFN- via JAK2-STAT1 signaling and predicts a poor survival in colorectal cancer". In: *Oncology Letters* 20.2 (2020), pp. 1127–1134. DOI: 10.3892/ol.2020.11647.

Appendices

A Radiation Modelling

When fractionally irradiated with a single-fraction dose I, the probability of survival of a single clonogenic cell is expressed as the exponential of the sum of linear and quadratic contributions to the surviving fraction:

$$S(I) = e^{-I(\alpha+\beta I)}, \tag{1}$$

where α and β are cell-specific radiosensitivity parameters. Radiation schedules consist of a set of instantaneous radiation events at times t_i over the period time of the treatment. As such, we represent the probability of non-survival by Dirac Delta function as input $\delta(t - t_i)$ where $\delta(t - t_i)$=1 when $t = t_i$ and 0, elsewhere:

$$\mu(I, t) = \left(1 - e^{-I(\alpha+\beta I)}\right) \sum_i \delta(t - t_i), \tag{2}$$

To capture the radiation resistance of GSCs relative to differentiated tumour cells, we assign distinct α and β values to each cell type, yielding separate non-survival probability functions $\mu_G(I, t)$ for differentiated tumour cells and $\mu_S(I, t)$ for GSCs. We also account for the damaging effect of radiation on immune cells. For simplicity, however, we assume identical α and β values across all immune cell types, giving a single non-survival function $\mu_{imm}(I, t)$.

B Full Model Description

Equation for Dendritic Cells (D). Glioma Stem Cells (GSCs) and differentiated tumour cells activate DCs by releasing HMGB-1 [16]. Radiation induced doomed cells activate DCs through the active release of antigens associated with their decay [108]. IFN-γ further enhances the DC maturation by increasing their CD86 surface receptors [80]. Treating D to be the effective density of antigen-presenting dendritic cells (reflecting both the abundance of cells and their maturation state), The dynamics of DCs are given by:

$$\begin{aligned} \frac{dD}{dt} = &\left(\lambda_{DG}\frac{G}{K_G + G} + \lambda_{DS}\frac{S}{K_S + S} + \lambda_{DC}\frac{C}{K_C + C}\right) \\ &\times \left(1 + \phi_{DI_\gamma}\frac{I_\gamma}{K_{I_\gamma} + I_\gamma}\right) - d_D D - \mu_{imm}(I, t) \end{aligned} \tag{3}$$

The first three terms on the right-hand side of the equation represent the activation rate of dendritic cells from a constant pool of immature dendritic cells by the differentiated tumour cells (G), glioma stem cells (GSCs) (S), and radiation-induced doomed cells (C), respectively. The terms enclosed in the second parentheses represent the amplification of DC activation under IFN-γ environment (I_γ), which acts on the existing activated DC population. Michaelis-Menten kinetics are used throughout these terms to account for the saturation of receptor binding that occurs at high ligand concentrations [22]. The final

two terms account for the natural death of the DCs as a result of their finite lifetime and death of DCs due to the ionizing radiation.

Equation for CD4$^+$ Th1 cells ($\mathbf{T_1}$). Naive CD4+ T cells differentiate into active Th1 cells (T_1) under stimulation by IL-12 while being suppressed by IL-10 and regulatory T cells (Tregs) [56]. The proliferation of activated Th1 cells is further amplified through IL-2-mediated clonal expansion [9]. Both T_1 activation and proliferation processes are inhibited by the PD-1-PD-L1 complex, reducing the overall functional activity of Th1 cells [91]. Hence T_1 dynamics are given by:

$$\begin{aligned}\frac{dT_1}{dt} = \Bigg(\lambda_{T_1 I_{12}} \times \frac{I_{12}}{K_{I_{12}} + I_{12}} \times \frac{K_{TI_{10}}}{K_{TI_{10}} + I_{10}} \times \frac{K_{TT_r}}{K_{TT_r} + T_r} \\ + \lambda_{T_1 I_2} T_1 \frac{I_2}{K_{I_2} + I_2}\Bigg) \times \frac{K_{TQ}}{K_{TQ} + Q} - d_{T_1} T_1 - \mu_{imm}(I, t)\end{aligned} \tag{4}$$

The first added term in the parentheses represents the generation of new Th1 cells from the pool of naive CD4+ T cells (T_{10}). The reservoir of continuously circulating naive cells is assumed to be constant. Activation by IL-12 (I_{12}) and suppression by IL-10 (I_{10}) and Tregs (T_r), expressed by Michaelis-Menten terms are multiplied to signify the codependence of activation and suppression events on the T_1 activation. The second added term in the parentheses represents the self-amplification of T_1 stimulated by IL-2 (I_2) secretion. The outer parentheses multiplier term represents PD-1-PD-L1 complex (Q) T_1 suppression, which acts upstream of both the activation and proliferation pathways. The final two terms account for the natural death of CD4+ Th1 cells and for the radiation-induced death.

Equation for CD8$^+$ cells ($\mathbf{T_8}$). Similarly to CD4+ Th1 cells, CD8+ cells are activated under IL-12 environment with the process being inhibited by IL-10 and Tregs [48, 94]. Activated CD8+ undergo clonal expansion stimulated by IL-2 released by CD4+ Th1 cells [50]. CD8+ cells' activity is inhibited by the PD-1PD-L1 complex [106]. Hence,

$$\begin{aligned}\frac{dT_8}{dt} = \Bigg(\lambda_{T_8 I_{12}} \times \frac{I_{12}}{K_{I_{12}} + I_{12}} \times \frac{K_{TI_{10}}}{K_{TI_{10}} + I_{10}} \times \frac{K_{TT_r}}{K_{TT_r} + T_r} \\ + \lambda_{T_8 I_2} T_8 \frac{I_2}{K_{I_2} + I_2}\Bigg) \times \frac{K_{TQ}}{K_{TQ} + Q} - d_{T_8} T_8 - \mu_{imm}(I, t)\end{aligned} \tag{5}$$

Where T_{80} is the constant reservoir of naive CD8+ T cells.

Equation for activated Tregs ($\mathbf{T_r}$). Naive CD4+ T cells differentiate into Tregs through stimulation by TGF-β by activating the Foxp3 gene [12]. Differentiation is further enhanced by the PD-1-PD-L1 complex which inhibits the Akt/mTOR pathway (Foxp3 suppressor) [26]. Hence the equation for T_r is given by:

$$\frac{dT_r}{dt} = \lambda_{T_r T_\beta} \frac{T_\beta}{K_{T_\beta} + T_\beta} + \lambda_{T_r Q} \frac{Q}{K_{TQ} + Q} - d_{T_r} T_r - \mu_{imm}(I, t) \tag{6}$$

In the first term, the outer parentheses multiplier (T_{10}) represents the constant reservoir of naive CD4+ cells. Inside the parentheses, the first term models the Tregs differentiation due to Foxp3 expression due to TGF-β (T_β) and the second term the gene expression due to PD-1-PD-L1 complex (Q). The final two terms account for the natural death of Tregs and their radiation-induced death, respectively.

Equation for MDSCs and M2 macrophages (M). In the GBM microenvironment, tumour-associated microglia and infiltrating macrophages are progressively polarised towards the immunosuppressive M2-like phenotype [10]. Immunosuppressive myeloid cells, including M2-polarised microglia and MDSCs, are considered as one population of M cells, as they exhibit very similar phenotypes and functions in the GBM microenvironment. Under the influence of cancer cells, M cells are recruited from myeloid cells circulating in the blood. This recruitment process is suppressed by IFN-γ released by CD4+ Th1 cells, as it polarizes myeloids towards the M1 phenotype, decreasing the M2/M1 macrophage population ratio [11]. Ionizing radiation (IR) induces the polarisation of monocytes toward non-inflammatory M2 macrophages [93, 92]. M cells are further polarised under TGF-β, IL-10, IL-1β environments [67]. The dynamics of M are modelled by:

$$\begin{aligned}\frac{dM}{dt} = \lambda_{\mathrm{MB}}\left(M_0 - M\right)^+ &\left(1 + \varepsilon_{\mathrm{MR}}\frac{\sum\limits_i R_i e^{-(t-t_i)/\tau_{MR}}}{K_{MR} + \sum\limits_i R_i e^{-(t-t_i)/\tau_{MR}}}\right) \\ &\times \left(\frac{G}{K_G + G} + \frac{S}{K_S + S}\right)\frac{K_{I_\gamma}}{K_{I_\gamma} + I_\gamma} + \lambda_{MT_\beta} M \frac{T_\beta}{K_{T_\beta} + T_\beta} \\ &+ \lambda_{MI_\beta} M \frac{I_\beta}{K_{I_\beta} + I_\beta} + \lambda_{MI_{10}} M \frac{I_{10}}{K_{I_{10}} + I_{10}} - d_M M - \mu_{imm}(I,t)\end{aligned} \tag{7}$$

The first term represents the development of non-inflammatory macrophages from myeloid cells; the first parentheses drives recruitment of monocytes from the available peripheral blood pool toward the immunosuppressive phenotype. M_0 is the source of monocytes from the blood and $(M - M_0)$ is the remaining unconverted monocyte supply. The second parentheses represent the radiation effects on the polarization effects of monocytes towards the M phenotype. The cumulative radiation signal $\sum_i R_i e^{-(t-t_i)/\tau_{MR}}$ sums the contributions of all previous radiation fractions, with each fraction R_i delivered in time t_i contributing a signal that decays exponentially with time constant τ_{MR} to reflect the gradual fading of the biological response to the successive fractions. Expression in the Michaelis-Menten form using K_{MR} as the half-saturation ensures the radiation effect saturates, such that maximum fold increase in polarization rate due to IR is $(1+\varepsilon_{MR})$ above the baseline. The third parentheses represent the cellular contribution of differentiated tumour cells (G) and GSCs (S) to driving M2 polarization and increasing the M phenotype. The IFN-γ (I_γ) inhibition expression is multiplied to represent the M1 driving signal of the cytokine. The second, third, and fourth terms symbolise the self-amplifying autocrine loop of M cells mediated by the secretion of TGF-β, IL-1β, and IL-10, respectively. The final two terms account for the natural death of M cells and their radiation-induced death, respectively.

Equation for glioma stem cells (S). Glioma stem cells are capable of self-renewal and differentiation into adult tumour cells. Self-renewal is achieved through symmetric division (one stem cell divides into two identical stem cells) while differentiation is achieved through asymmetric division (one stem cell divides to make one stem cell and one differentiated tumour cell) [29, 95]. In particular, it is only the symmetric division that changes the size of the stem cell population. IR has been shown to increase the likelihood of symmetric division in GSCs [29]. We assume a logistic growth through symmetric division of GSCs with a carrying capacity K_{SG} shared between GSCs (S) and differentiated tumour cells (G) to account for the shared physical space of all cancer cells. IL-1β can promote

self-proliferation in GSCs through NF-κB signalling [99]. GSCs are killed by CD8+ (T_8) cells and radiation. The dynamics of S take the form:

$$\begin{aligned}\frac{dS}{dt} = &\left(p_{S0} + \varepsilon_p \frac{\sum_i R_i e^{-(t-t_i)/\tau_p}}{K_p + \sum_i R_i e^{-(t-t_i)/\tau_p}}\right) \lambda_S S \left(1 - \frac{S+G}{K_{SG}}\right) \\ &\times \left(1 + \lambda_{SI_\beta} \frac{I_\beta}{K_{I_\beta} + I_\beta}\right) - \eta_{ST_8} T_8 \frac{S}{K_S + S} - \mu_S(I,t) S\end{aligned} \tag{8}$$

The first term represents the proliferation of GSCs. The first parentheses give a value for the probability that GSC division is symmetric, $p_s(t)$. The cumulative radiation signal $\sum_i R_i e^{-(t-t_i)/\tau_p}$ accumulates contributions from all past radiation fractions with exponential decay of the constant τ_p. As such, the symmetric division fraction ranges from the baseline p_{s0} in the absence of radiation to the experimentally shown maximum value of $p_{s0} + \varepsilon_p$ in case of high IR doses [29]. The second parentheses represent the S population growth due to the logistic growth and the third parentheses the growth due to the IL-1β driven self-proliferation.The second term represents the killing of GSCs by T_8 cells with a killing rate η_{ST_8}. $\mu_S(I,t)$ is the death rate by radiation (turning cells into doomed cancer cells, compartment C).

Equation for bulk differentiated tumour cells (G). Differentiated tumour cells increase in numbers either through self proliferation or through differentiation of GSCs during asymmetric division. We assume differentiated tumour cells exhibit a similar growth mode to GSCs (logistic) with a carrying capacity K_{SG}. Differentiated tumour cells are killed by CD8+ (T_8) cells and radiation. The dynamics of G take the form:

$$\begin{aligned}\frac{dG}{dt} = &\lambda_G G \left(1 - \frac{S+G}{K_{SG}}\right) + \left(1 - p_{S0} - \varepsilon_p \frac{\sum_i R_i e^{-(t-t_i)/\tau_p}}{K_p + \sum_i R_i e^{-(t-t_i)/\tau_p}}\right) \lambda_S S \\ &\times \left(1 - \frac{S+G}{K_{SG}}\right) - \eta_{GT_8} T_8 \frac{G}{K_G + G} - d_G G - \mu_G(I,t) G\end{aligned} \tag{9}$$

The first term represents the proliferation of G cells that follows logistic growth. The second term represents the increase in G due to asymmetric division of GSCs. The parenthesis in the term, which are the complement of the symmetric division fraction in the GSC equation and that can be written in the form $(1 - p_s(t))$, express the fraction of asymmetric divisions of GSCs. The third term represents the killing of differentiated tumour cells by T_8 cells with a killing rate η_{GT_8}. $\mu_G(I,t)$ is the death rate by radiation (turning cells into doomed cancer cells, compartment C), and d_G is the natural death rate of G cells.

Equation for radiation caused doomed tumour cells (C). Instead of being immediately considered dead, radiation damaged GSCs and differentiated tumour cells are still important for consideration as they actively release antigens during their decay [6]. These antigens play a role in the activation of dendritic cells and their enhancement. Hence, C cells are modelled using:

$$\frac{dC}{dt} = \mu_S(I,t) S + \mu_G(I,t) G - d_C C \tag{10}$$

The first two terms represent the killing rate of GSCs and differentiated tumour cells by radiation, respectively. The last term represents the decay of the doomed cells as they quickly disappear.

Equation for IL-12 ($\mathbf{I_{12}}$). The proinflammatory cytokine IL-12 is produced and secreted by activated dendritic cells [34]. Radiation suppresses IL-12 production by DCs through the inhibition of NF-κB driven IL-12 transcription [55]. So the IL-12 (I_{12}) equation is:

$$\frac{dI_{12}}{dt} = \lambda_{I_{12}D}\frac{D}{1+\left(\sum_i \frac{R_i}{t_i - t_{(i-1)}}\right)/K_{I_{12}R}} - d_{I_{12}}I_{12} \tag{11}$$

The first term represents the production of IL-12 by DCs. We assume radiation decreases the production of the cytokine by a factor of $\left[1+\left(\sum_i \frac{R_i}{t_i - t_{(i-1)}}\right)/K_{I_{12}R}\right]$. The sum term represents the average total radiation dose rate to reflect the biological effects of the intensity of the radiation therapy on the IL-12 suppression. Notably, the IL-12 production term does not use Michaelis-Menten saturation because IL-12 secretion is treated as a constitutive output of mature DCs rather than a receptor-mediated process with binding saturation. The last term represents the natural enzymatic degradation that the cytokine undergoes.

Equation for IL-2 ($\mathbf{I_2}$). IL-2 is produced by activated CD4+ (T_1) cells [59]. Thus, its equation is:

$$\frac{dI_2}{dt} = \lambda_{I_2T_1}T_1 - d_{I_2}I_2 \tag{12}$$

The first term represents the production of IL-2 by T_1 cells and the second term the natural degradation of IL-2.

Equation for TGF-$\boldsymbol{\beta}$ ($\boldsymbol{T_\beta}$). The immunosuppressive cytokine TGF-β is produced by tumour cells (GSCs and differentiated cells), Tregs and MDSCs (M phenotype expressing cells) [81]. Additionally, TGF-β is particularly produced by fibroblast cells present in the tumour micro-environment [61]. Fibroblasts respond to radiation-induced tissue damage by secreting TGF-$\boldsymbol{\beta}$ as part of the wound healing response [65, 92]. The dynamics of TGF-$\boldsymbol{\beta}$ are modelled by:

$$\frac{dT_\beta}{dt} = \lambda_{T_\beta S}S + \lambda_{T_\beta G}G + \lambda_{T_\beta T_r}T_r + \lambda_{T_\beta M}M + f\cdot(\lambda_{T_\beta f0} + \lambda_{T_\beta frad}\cdot\mu_G(I,t)) - d_{T_\beta}T_\beta \tag{13}$$

The first four terms represent the production of TGF-$\boldsymbol{\beta}$ by GSCs, differentiated tumour cells, Tregs, and M cells, respectively. The fifth term represents the fibroblast radiation-induced secretion of TGF-$\boldsymbol{\beta}$. The fibroblast population, f, is treated as constant for simplicity's sake as fibroblast dynamics are much slower than immune and tumour cell dynamics. We take the TGF-$\boldsymbol{\beta}$ production by fibroblasts to be proportional to the IR effect on the differentiated cells $\mu_G(I,t)$ as a measure of radiation-induced tissue damage. The final term represents the natural degradation of TGF-$\boldsymbol{\beta}$.

Equation for IL-10 ($\mathbf{I_{10}}$). The anti-inflammatory cytokine IL-10 is produced by tumour cells (GSCs and differentiated cells) and by MDSCs (M phenotype expressing cells) [82]. Thus, the equation for IL-10 is:

$$\frac{dI_{10}}{dt} = \lambda_{I_{10}M}M - d_{I_{10}}I_{10} \tag{14}$$

The first three terms represent the production of IL-10 by GSCs, differentiated tumour cells, and M cell, respectively. The final term represents the natural degradation of IL-10.

Equation for IL-1β (I_β). The pro-inflammatory cytokine IL-1β is produced by GSCs and M cells [66]. Hence,

$$\frac{dI_\beta}{dt} = \lambda_{I_\beta S} S + \lambda_{I_\beta M} M - d_{I_\beta} I_\beta \tag{15}$$

The first two terms represent the production of IL-1β by GSCs and M cells, respectively. The final term represents the natural degradation of IL-1β.

Equation for IFN-γ (I_γ). The pro-inflammatory cytokine IFN-γ is produced and secreted by CD4+ (T_1) and CD8+ (T_8) cells [73]. Its equation is thus:

$$\frac{dI_\gamma}{dt} = \lambda_{I_\gamma T_1} T_1 + \lambda_{I_\gamma T_8} T_8 - d_{I_\gamma} I_\gamma \tag{16}$$

The first two terms represent the secretion by T_1 and T_8 cells, respectively. The final term represents the natural degradation of IFN-γ.

Equation for PD-1 (P). CD4+ and CD8+ cells express PD-1 on their surface, with the density of surface proteins per unit cell mass for the two cells types to be equal [86]. Tregs also express PD-1, however, it is assumed to be smaller by a factor of θ_r compared to the T cells. Denoting the ratio between the mass of one PD-1 protein and one T cell to be ρ_P, then:

$$P = \rho_P \left(T_1 + T_8 + \theta_r T_r\right) \tag{17}$$

Equations for PD-L1 (L). PD-L1 is expressed by MDSCs as wells as tumour cells (GSCs and differentiated cells) [86, 54]. G and S cells are assumed to have smaller PD-L1 expressions by factors of θ_G, and θ_S, respectively, than M cells. PD-L1 is upregulated by IFN-γ through JAK1/JAK2-STAT1-IRF signalling [110]. Denoting the ratio between the mass of one PD-L1 protein and one M cell to be ρ_L, then:

$$L = \rho_L \left(M + \theta_G G + \theta_S S\right) \left(1 + \phi_{I_\gamma L} \frac{I_\gamma}{K_{I_\gamma} + I_\gamma}\right) \tag{18}$$

Where the first parenthesised term represents the number of PD-L1 proteins in all cell types, and the second parenthesised term the upregulation of PD-L1 by IFN-γ expressed in the Michaelis-Menten form. The coefficient ρ_L is constant when no anti-PD-L1 drug is administered. Under such case, the dynamics of L can be tracked by differentiating L with respect to time:

$$\begin{aligned} \frac{dL}{dt} = &\frac{L}{M + \theta_G G + \theta_S S} \left(\frac{dM}{dt} + \theta_G \frac{dG}{dt} + \theta_S \frac{dS}{dt}\right) \\ &+ \frac{L \times \phi_{I_\gamma L} \times K_{I_\gamma L}}{\left(1 + \phi_{I_\gamma L} \frac{I_\gamma}{K_{I_\gamma L} + I_\gamma}\right) \left(K_{I_\gamma L} + I_\gamma\right)^2} \frac{dI_\gamma}{dt} - \mu_{LA} L A \end{aligned} \tag{19}$$

$$\frac{dL}{dt} = \rho_L \Bigg[\left(\frac{dM}{dt} + \theta_G \frac{dG}{dt} + \theta_S \frac{dS}{dt} \right) \left(1 + \phi_{I_\gamma L} \frac{I_\gamma}{K_{I_\gamma} + I_\gamma} \right) + \left(\phi_{I_\gamma L} \frac{K_{I_\gamma L}}{(K_{I_\gamma L} + I_\gamma)^2} \frac{dI_\gamma}{dt} \right) (M + \theta_G G + \theta_S S) \Bigg] - \mu_{LA} L A \tag{20}$$

The first two terms are the result of the simple differential solution of L. The last term is added explicitly physical depletion of PD-L1 by anti-PD-L1 drug (A) binding to PD-L1 molecules.

Equation for an anti-PD-L1 administered (A). An anti-PD-L1 drug is considered to be administered to the blood at j doses denoted by γ_{A_j}. The brain-blood-barrier (BBB) permeability is taken into account when considering the drug entrance into the tumour microenvironmnet from circulation in the blood. Ionizing radiation impairs the integrity of the BBB, increasing its permeability for some period of time before its normal function is restored [38, 97]. The drug A is depleted in the process of $PD - L1$ blockage. Hence, the drug's eqaution is defined as:

$$\frac{dA}{dt} = \sum_j \left[\gamma_{A_j} e^{\alpha_0 (t - t_j)} H\left(t - t_j\right) \mathcal{BBB}(t) \right] - \mu_{LA} L A - d_A A \tag{21}$$

$$\mathcal{BBB}(t) = \mathcal{B}_0 + \varepsilon_{\mathcal{B}R} \sum_j \left[\frac{t - t_j}{\tau_{\mathcal{B}}} e^{1 - (t - t_j)/\tau_{\mathcal{B}}} \right] H\left(t - t_j\right) \tag{22}$$

The first term represents the delivery of the drug to the tumour microenvironmnet. In humans, anti-PD-L1 (e.g., pembrolizumab) has half life of about 18 days. Hence, the effective amount of the drug in the blood at any time $t > t_j$ following administration is $\gamma_{A_j} e^{\alpha_0 (t - t_j)}$ where $\alpha_0 = \frac{ln2}{18}$. The expression is represented by the Heaviside step function as input where $H\left(t - t_i\right) = 1$ at $t > t_j$ (administration times), and 0 elsewhere. The BBB permeability, with the baseline value $\mathcal{B}_0$ value, increases according to a Michaelis-Menten form of the cumulative decaying radiation signal $\sum_i R_i e^{-(t - t_i)/\tau_{\mathcal{B}R}}$ to a maximum values of $\mathcal{B}_0 + \varepsilon_{\mathcal{B}R}$. The second term represents the depletion of drug A in the process of PD-L1 blockage. The last term represents the degradation of the drug in the tumour microenvironment.

Equations for the PD-1-PD-L1 complex (Q). PD-L1 from differentiated tumour cells, GSCs, and MDSCs combines with PD-1 on the plasma membrane of T cells to form the PD-1-PD-L1 complex (Q). Denoting the association rate of Q as α_{PL} and the dissociation rate as d_Q, the reaction of the complex formation can be written as:

$$P + L \underset{d_Q}{\overset{\alpha_{PL}}{\rightleftharpoons}} Q \tag{23}$$

The half life of Q is less than 1 second [70]. Hence we approximate that the dynamical equation for Q follows quasi steady state:

$$\alpha_{PL} P L = d_Q Q \tag{24}$$

Or that Q is:

$$Q = \frac{\alpha_{PL}}{d_Q} P L \tag{25}$$

The concentration Q is involved in the model equations only through the factors $\frac{K_{TQ}}{K_{TQ}+Q}$ and $\frac{Q}{K_{TQ}+Q} = 1 - \frac{K_{TQ}}{K_{TQ}+Q}$. Hence, we can assume $\frac{\alpha_{PL}}{d_Q} = 1$, and thus $Q = PL$.

C Parameter Estimation

From results reported in [71] and assuming mass of singular cell regardless of type is 5×10^{-10} g, we estimate the steady-state cellular masses (denoted by *) in absence of therapy or treatment to be: $T_1^* = 3.4 \times 10^{-2}$ g; $T_8^* = 4.2 \times 10^{-2}$ g; $T_r^* = 4.3 \times 10^{-3}$ g; $D^* = 1.7 \times 10^{-2}$ g; $M^* = 0.425$ g; $S^* = 0.285$ g. Similarly, the steady-state cytokine levels are estimated to be: $IL\text{-}12^* = 1.3 \times 10^{-8}$ g [1]; $IL\text{-}10^* = 1.3 \times 10^{-7}$ g [43]; $IFN\text{-}\gamma^* = 4.3 \times 10^{-7}$ g [43]; $IL\text{-}2^* = 4.7 \times 10^{-7}$ g [96]; $TGF\text{-}\beta^* = 5.9 \times 10^{-7}$ g [58]; $IL\text{-}1\beta^* = 1.7 \times 10^{-9}$ g [43].

Following [4], the carrying capacity of the tumour is set at $K_{SG} = 19.36$ g, and the proliferation rate of differentiated tumour cells is set to $\lambda_G = 0.192$ day^{-1}, following [90] and refining slightly after testing. We follow [29, 104] in assuming that the GSC division rate is similar to that of non-GSC cells, so $\lambda_S = \lambda_G = 0.192$ day^{-1}. Following simulation results in [51], we set G^* to be $0.8 \times K_{SG}$, $G^* = 15.49$ g. The peripheral monocyte pool mass M_0 is estimated from the same source to be 0.594 g, assuming its population is comparable to that of $CD68^+$ cells, since CD68 provides a reasonable basis for approximating infiltrating myeloid cells. Drawing on results from [42], we estimate the fibroblast mass f to constitute 23% of the combined fibroblast and G^* mass, corresponding to a value of 4.62 g. We applied the steady-state assumptions to the equations for cytokine dynamics (11)-(16) and estimated the cytokine production rates through the established steady-state cell and cytokine levels. For example, consider the steady state of the equation for $IFN\text{-}\gamma$:

$$\lambda_{I_\gamma T_1} T_1^* + \lambda_{I_\gamma T_8} T_8^* - d_{I_\gamma} I_\gamma^* = 0$$

We take the equilibrium values of T_1, T_8, I_γ mentioned previously. Based on findings in [75], we assume that the production rate of $IFN\text{-}\gamma$ by CD4+ cells is three times the production rate of the cytokine by CD8+ cells. Consequently,

$$\begin{aligned}\lambda_{I_\gamma T_8} = \frac{1}{3}\lambda_{I_\gamma T_1} &= \frac{d_{I_\gamma} I_\gamma^*}{3T_1^* + T_8^*} \\ &= \frac{2.16 \times 4.3 \times 10^{-7}}{3 \times 3.4 \times 10^{-2} + 4.2 \times 10^{-2}} = 6.49 \times 10^{-6} day^{-1}\end{aligned}$$

Parameters for other cytokines and cells are estimated following a similar approach using the following production rate ratio assumptions from reported experimental results. $\lambda_{MI_\beta} = 1.5 \times \lambda_{SI_\beta}$ [13]; $\lambda_{T_\beta M} = 5.4 \times \lambda_{T_\beta G} = 5.4 \times \lambda_{T_\beta T_r} = 0.6 \times \lambda_{T_\beta S}$ [63, 62, 103]; $\lambda_{T_\beta f_0} = 2 \times \lambda_{T_\beta G} = 0.2 \times \lambda_{T_\beta f_{rad}}$ [87, 63]; $\lambda_{DC} = 2.1 \times \lambda_{DG} = 1.9 \times \lambda_{DS}$ [28, 44].

Following [4], we set the killing rate of the bulk cancer cells by $CD8^+$ T cells to $\eta_{GT_8} = 2.88$ day^{-1}. Based on [8], which found that stem-like cells were approximately equally susceptible to $CD8^+$ CTL-mediated killing as differentiated tumour cells, we set $\eta_{ST_8} = \eta_{GT_8}$.

To estimate ϕ_{DI_γ}, the dimensionless maximum fold-enhancement of DC activation by IFN-γ, we draw on findings from [7], where treatment with IFN-γ increased the percentage of activated ($CD86^+$) dendritic cells by approximately 41.7-fold relative to untreated controls. Accordingly, we set $\phi_{DI_\gamma} = 40.7$.

The enhancement of PD-L1 expression by IFN-γ was estimated using results from [20], where exposure to IFN-γ increased PD-L1 expression on cancer cells by approximately 3-fold. Solving for $\phi_{I_\gamma L}$ gives:

$$\begin{aligned} 1 + \phi_{I_\gamma L}\frac{I_\gamma}{K_{I_\gamma} + I_\gamma} &= 3 \\ \phi_{I_\gamma L} = \frac{2(K_{I_\gamma} + I_\gamma)}{I_\gamma} &= \frac{2 \times (1.89 \times 10^{-7} + 4.3 \times 10^{-7})}{4.3 \times 10^{-7}} = 2.87 \end{aligned} \tag{26}$$

When estimating the decay time constant τ_{MR} in Equation (7), we drew on results presented in [45], which showed that the relative increase in TAMs persisted for 13 days before returning to levels comparable to unirradiated controls as tumour growth resumed. Taking "comparable levels" to correspond to a 95% decline in the radiation-induced effect, τ_{MR} is estimated as:

$$\begin{aligned} \frac{Rs(13)}{Rs(0)} &= e^{-13/\tau_{MR}} = 0.05 \\ \tau_{MR} &= -\frac{13}{ln(0.05)} = 4.3 \; days \end{aligned} \tag{27}$$

A similar approach was used to estimate the decay time constants τ_p and τ_B appearing in Equations (8) and (22), respectively. The half-saturation radiation parameters K_{MR} and K_p were estimated based on findings reported in [29]: half-maximal radiation-induced enhancement of macrophage activity was shown to be achieved at 1 Gy (Gy is the unit of measurement for radiation and 1 Gy is equal to 1 joule of absorbed energy per kilogram of tissue), while maximal enhancement of symmetric GSC division occurred at a single dose of 3 Gy. Accordingly, these parameter values were set to $K_{MR} = 1$ Gy and $K_p = 3$ Gy.

D Model Parameters

Table 1: Summary of parameter values

Notation	Description	Value	Refs.
Baseline Masses & Cellular Pools			
M_0	Peripheral monocyte pool mass	0.594 g	Estimated
f	Constant fibroblast mass	4.62 g	Estimated
Growth, Activation, & Production Rates			
λ_{DG}	Activation rate of DCs by bulk tumour G	2.00×10^{-7} day^{-1}	Estimated
λ_{DS}	Activation rate of DCs by GSCs S	2.20×10^{-7} day^{-1}	Estimated
λ_{DC}	Activation rate of DCs by doomed cells C	4.19×10^{-7} day^{-1}	Estimated
ϕ_{DI_γ}	DC fold-enhancement by IFN-γ	40.7	Estimated
$\lambda_{T_1 I_{12}}$	Activation rate of CD4$^+$ T cells by IL-12	2.84×10^{-3} day^{-1}	Estimated
$\lambda_{T_1 I_2}$	Activation rate of CD4$^+$ T cells by IL-2	7.09×10^{-3} day^{-1}	Estimated

Continued on next page

Table 1: Summary of parameter values *(continued)*

Notation	Description	Value	Refs.
$\lambda_{T_8 I_{12}}$	Activation rate of CD8$^+$ T cells by IL-12	2.53×10^{-3} day^{-1}	Estimated
$\lambda_{T_8 I_2}$	Activation rate of CD8$^+$ T cells by IL-2	7.09×10^{-3} day^{-1}	Estimated
$\lambda_{T_r T_\beta}$	Activation rate of Tregs by TGF-β	8.35×10^{-3} day^{-1}	Estimated
$\lambda_{T_r Q}$	Activation rate of Tregs by PD-1–PD-L1	1.67×10^{-3} day^{-1}	Estimated
λ_{MB}	Recruitment/Activation rate of MDSCs	1.67×10^{-2} day^{-1}	Estimated
λ_{MT_β}	Activation rate of MDSCs by TGF-β	5.57×10^{-3} day^{-1}	Estimated
λ_{MI_β}	Activation rate of MDSCs by IL-1β	1.39×10^{-3} day^{-1}	Estimated
$\lambda_{MI_{10}}$	Activation rate of MDSCs by IL-10	8.35×10^{-3} day^{-1}	Estimated
p_{S0}	Baseline probability of symmetric division	0.35	Estimated
λ_S	Growth/division rate of GSCs	0.192 day^{-1}	Estimated
λ_{SI_β}	Fold-enhancement of GSCs by IL-1β	0.051	Estimated
η_{ST_8}	Killing rate of GSCs by CD8$^+$ T cells	2.88 day^{-1}	Estimated
λ_G	Growth rate of bulk tumour cells	0.192 day^{-1}	[90]
η_{GT_8}	Killing rate of bulk cells by CD8$^+$ T cells	2.88 day^{-1}	[4]
$\lambda_{I_{12}D}$	Production rate of IL-12 by DCs	1.12×10^{-6} day^{-1}	Estimated
$\lambda_{I_2 T_1}$	Production rate of IL-2 by CD4$^+$ T cells	3.31×10^{-5} day^{-1}	Estimated
$\lambda_{T_\beta S}$	Production rate of TGF-β by GSCs	2.89×10^{-5} day^{-1}	Estimated
$\lambda_{T_\beta G}$	Production rate of TGF-β by bulk cells	3.35×10^{-6} day^{-1}	Estimated
$\lambda_{T_\beta T_r}$	Production rate of TGF-β by Tregs	3.35×10^{-6} day^{-1}	Estimated
$\lambda_{T_\beta M}$	Production rate of TGF-β by MDSCs	1.81×10^{-5} day^{-1}	Estimated
$\lambda_{T_\beta f0}$	Production rate of TGF-β by fibroblasts	6.70×10^{-6} day^{-1}	Estimated
$\lambda_{T_\beta frad}$	Radiated production rate of TGF-β by fibroblasts	3.42×10^{-5} day^{-1}	Estimated
$\lambda_{I_{10}M}$	Production rate of IL-10 by MDSCs	2.62×10^{-6} day^{-1}	Estimated
$\lambda_{I_\beta S}$	Production rate of IL-1β by GSCs	1.25×10^{-8} day^{-1}	Estimated
$\lambda_{I_\beta M}$	Production rate of IL-1β by MDSCs	1.87×10^{-8} day^{-1}	Estimated
$\lambda_{I_\gamma T_1}$	Production rate of IFN-γ by CD4$^+$	1.95×10^{-5} day^{-1}	Estimated
$\lambda_{I_\gamma T_8}$	Production rate of IFN-γ by CD8$^+$	6.49×10^{-6} day^{-1}	Estimated
Death & Degradation Rates			
d_D	Death rate of DCs	0.1 day^{-1}	[53]
d_{T_1}	Death rate of CD4$^+$ T cells	0.197 day^{-1}	[27]
d_{T_8}	Death rate of CD8$^+$ T cells	0.18 day^{-1}	[53]
d_{T_r}	Death rate of Tregs	0.2 day^{-1}	[64]
d_M	Death rate of MDSCs	0.015 day^{-1}	[37]
d_G	Natural death rate of bulk cells	0.17 day^{-1}	[104]
d_C	Clearance rate of doomed cells	1.41 day^{-1}	[104]
$d_{I_{12}}$	Degradation rate of IL-12	1.38 day^{-1}	[27]
d_{I_2}	Degradation rate of IL-2	2.376 day^{-1}	[53]
d_{T_β}	Degradation rate of TGF-β	166.32 day^{-1}	[46]
$d_{I_{10}}$	Degradation rate of IL-10	8.32 day^{-1}	[53]
d_{I_β}	Degradation rate of IL-1β	6.65 day^{-1}	[36]
d_{I_γ}	Degradation rate of IFN-γ	2.16 day^{-1}	[18]

Continued on next page

Table 1: Summary of parameter values *(continued)*

Notation	Description	Value	Refs.
Half-Saturation Constants & Carrying Capacities			
K_G	Half-saturation of bulk tumour cells	7.339 g	[4]
K_S	Half-saturation of GSCs	24.30 g	[31]
K_C	Half-saturation of doomed tumour cells	7.339 g	[4]
K_{I_γ}	Half-saturation of IFN-γ	1.890×10^{-7} g	[89]
$K_{I_{12}}$	Half-saturation of IL-12	2.700×10^{-9} g	[72]
$K_{TI_{10}}$	Inhibition of T cells by IL-10	4.050×10^{-8} g	[53]
K_{TT_r}	Inhibition of T cells by Tregs	3.375×10^{-3} g	[53]
K_{I_2}	Half-saturation of IL-2	6.415×10^{-10} g	[102]
K_{T_β}	Half-saturation of TGF-β	5.561×10^{-7} g	[17]
K_{I_β}	Half-saturation of IL-1β	2.627×10^{-9} g	[68]
$K_{I_{10}}$	Half-saturation of IL-10	8.102×10^{-8} g	[49]
K_{SG}	Shared carrying capacity of GSCs & Bulk	19.36 g	[33]
PD-1/PD-L1 Checkpoint & Drug Parameters			
ρ_P	Expression coefficient of PD-1 in T cells	2.49×10^{-7}	[51]
ρ_L	Expression coefficient of PD-L1	3.25×10^{-8}	[51, 52]
θ_r	Fraction of PD-1 in Tregs	0.8	[51]
θ_G	Fraction of PD-L1 in bulk tumour cells	1	[51]
θ_S	Fraction of PD-L1 in GSCs	1.2	Estimated
$\phi_{I_\gamma L}$	Enhancement of PD-L1 by IFN-γ	2.87	Estimated
K_{TQ}	Inhibition of T cells by complex Q	9.190×10^{-15} g^2	[109]
μ_{LA}	Blocking rate of PD-L1 by anti-PD-L1	5.333×10^6 g^{-1} day^{-1}	[51]
d_A	Clearance rate of anti-PD-L1 drug	0.046 day^{-1}	[51]
Radiation & BBB Permeability Parameters			
α_G	LQ radiosensitivity for bulk cells	0.173 Gy^{-1}	[30]
β_G	LQ radiosensitivity for bulk cells	0.0184 Gy^{-2}	[30]
α_S	LQ radiosensitivity for GSCs	0.00029 Gy^{-1}	[69]
β_S	LQ radiosensitivity for GSCs	0.00002 Gy^{-2}	[69]
α_{imm}	LQ radiosensitivity for immune cells	0.19 Gy^{-1}	[79]
β_{imm}	LQ radiosensitivity for immune cells	0.14 Gy^{-2}	[79]
K_{MR}	Half-saturation of radiation on MDSCs	1 Gy	Estimated
K_p	Half-saturation of radiation on p_{S0}	3 Gy	Estimated
τ_{MR}	Decay time constant of radiation on MDSCs	4.3 days	Estimated
τ_p	Decay time constant of radiation on p_{S0}	2.0 days	Estimated
ε_{MR}	Max radiation enhancement on MDSCs	0.75	Estimated
ε_p	Max radiation enhancement on p_{S0}	0.4	Estimated
$K_{I_{12}R}$	Half-saturation of dose rate on IL-12	3.3 Gy/day	Estimated
B_0	Baseline dimensionless BBB permeability	0.002	Estimated
ε_{BR}	Max radiation enhancement on BBB	0.002	Estimated
τ_{BR}	Delay time constant of radiation on BBB	8 days	Estimated

It should be noted that parameter values taken from the literature were rescaled to fit the units of the model, since the constant-volume assumption employed here allows

densities to be converted directly to mass.

E Treatment Outcome Measures

We let $F(t) = G(t) + S(t)$ denote total tumour mass (bulk cells plus GSCs), and let t_{treat} denote the time at which treatment begins, with $F_{pre} = F(t_{treat})$ the tumour mass at treatment onset. Let $t_{min} = \arg\min_{t \geq t_{treat}} F(t)$ denote the time at which the tumour reaches its minimum size (known as the nadir) following treatment, and let $F_{min} = F(t_{min})$. We define the progression threshold F^* as the tumour mass halfway between the nadir and the pre-treatment size:

$$F^* = F_{min} + \frac{1}{2}\left(F_{pre} - F_{min}\right) \tag{28}$$

Time to progression (TTP) is then defined as the elapsed time, following the nadir, until the tumour mass first returns to this threshold:

$$TTP = t_{prog} - t_{min}, \qquad \text{where} \quad t_{prog} = \min\{t > t_{min} : F(t) \geq F^*\} \tag{29}$$

Maximum tumour reduction (MTR) quantifies the greatest relative decrease in tumour mass achieved following treatment, expressed as a percentage of the pre-treatment tumour size:

$$MTR = \frac{F_{pre} - F_{min}}{F_{pre}} \times 100\% \tag{30}$$

Tumour burden reduction (TBR) quantifies the cumulative reduction in tumour mass attributable to treatment, integrated over a fixed evaluation window $[t_{treat}, t_{end}]$ that spans the treatment period and subsequent follow-up. It is defined as the area between the untreated and treated tumour growth curves:

$$TBR = \int_{t_{treat}}^{t_{end}} F_{untreated}(t)\, dt - \int_{t_{treat}}^{t_{end}} F_{treated}(t)\, dt \tag{31}$$

Where $F_{untreated}(t)$ is the tumour mass trajectory under no treatment, $F_{treated}(t)$ is the tumour mass trajectory under the schedule being evaluated, and t_{end} is a fixed evaluation horizon, selected to be long enough to capture tumour relapse across all schedules considered, yet short enough to avoid excessive overlap between $F_{treated}(t)$ and $F_{untreated}(t)$ after relapse, which would otherwise weaken the discriminative power of the TBR metric.